

Journal Pre-proof



Single-cell and spatial transcriptomics characterisation of the immunological landscape in the healthy and PSC human liver

Tallulah S. Andrews, Diana Nakib, Catia T. Perciani, Xue Zhong Ma, Lewis Liu, Erin Winter, Damra Camat, Sai W. Chung, Patricia Lumanto, Justin Manuel, Shantel Mangroo, Bettina Hansen, Bal Arpinder, Cornelia Thoeni, Blayne Sayed, Jordan Feld, Adam Gehring, Aliya Gulamhusein, Gideon M. Hirschfield, Amanda Ricciuto, Gary D. Bader, Ian D. McGilvray, Sonya MacParland

PII: S0168-8278(24)00003-5

DOI: <https://doi.org/10.1016/j.jhep.2023.12.023>

Reference: JHEPAT 9447

To appear in: *Journal of Hepatology*

Received Date: 1 February 2023

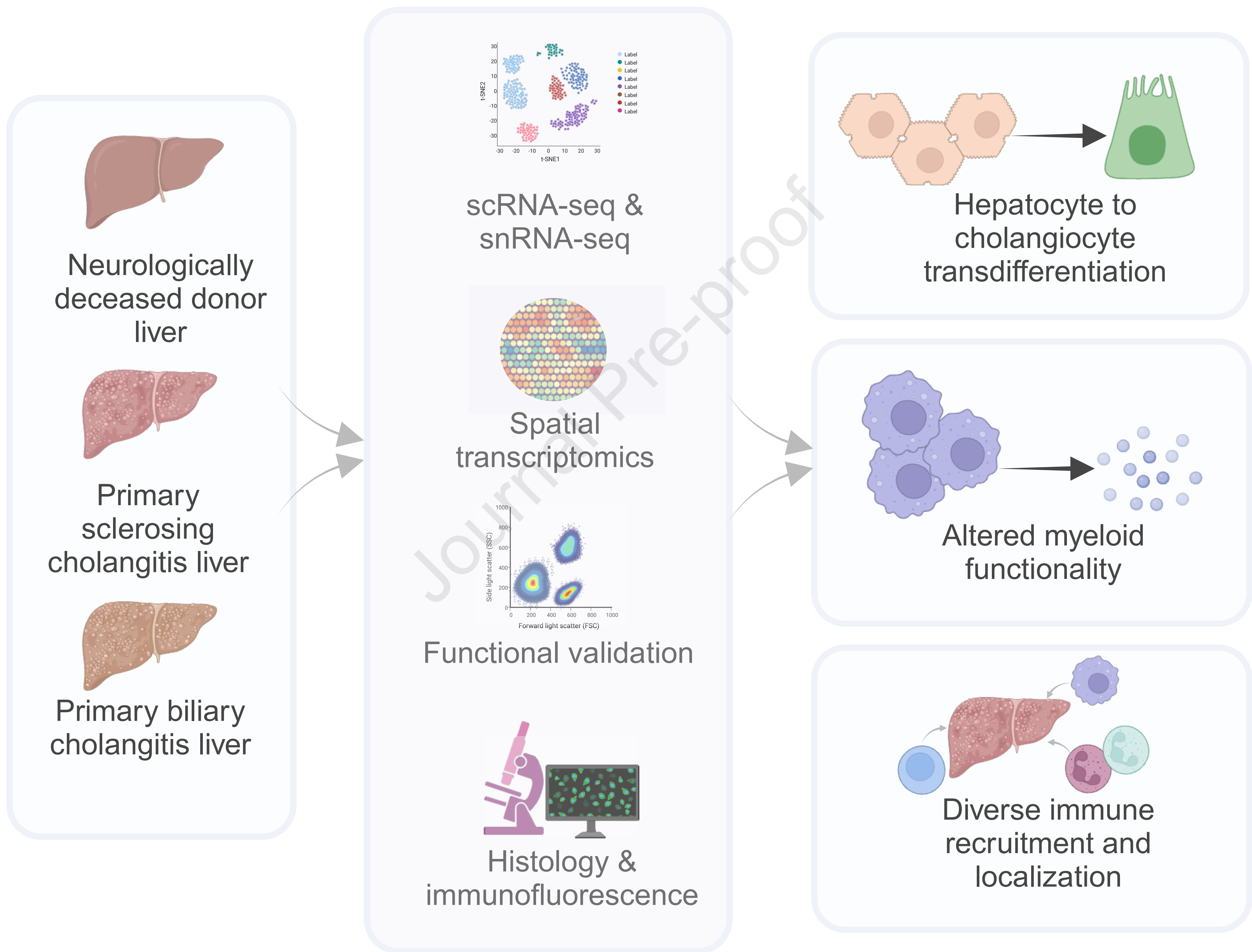
Revised Date: 13 December 2023

Accepted Date: 20 December 2023

Please cite this article as: Andrews TS, Nakib D, Perciani CT, Ma XZ, Liu L, Winter E, Camat D, Chung SW, Lumanto P, Manuel J, Mangroo S, Hansen B, Arpinder B, Thoeni C, Sayed B, Feld J, Gehring A, Gulamhusein A, Hirschfield GM, Ricciuto A, Bader GD, McGilvray ID, MacParland S, Single-cell and spatial transcriptomics characterisation of the immunological landscape in the healthy and PSC human liver, *Journal of Hepatology* (2024), doi: <https://doi.org/10.1016/j.jhep.2023.12.023>.

This is a PDF file of an article that has undergone enhancements after acceptance, such as the addition of a cover page and metadata, and formatting for readability, but it is not yet the definitive version of record. This version will undergo additional copyediting, typesetting and review before it is published in its final form, but we are providing this version to give early visibility of the article. Please note that, during the production process, errors may be discovered which could affect the content, and all legal disclaimers that apply to the journal pertain.

© 2024 The Author(s). Published by Elsevier B.V. on behalf of European Association for the Study of the Liver.



Title: Single-cell and spatial transcriptomics characterisation of the immunological landscape in the healthy and PSC human liver

Short Title: Mapping the healthy and diseased liver

Tallulah S. Andrews^{1,2,3#}, Diana Nakib^{1,4#}, Catia T. Perciani^{1,4,5}, Xue Zhong Ma¹, Lewis Liu^{1,4}, Erin Winter¹, Damra Camat^{1,4}, Sai W. Chung^{1,4}, Patricia Lumanto^{1,4}, Justin Manuel¹, Shantel Mangroo⁶, Bettina Hansen^{7,8}, Bal Arpinder¹, Cornelia Thoeni⁵, Blayne Sayed¹, Jordan Feld⁷, Adam Gehring^{4,7}, Aliya Gulamhusein⁷, Gideon M Hirschfield⁷, Amanda Ricciuto⁶, Gary D. Bader^{9*}, Ian D. McGilvray^{1*}, Sonya MacParland^{1,4,5*}

Affiliations:

¹ Ajmera Transplant Centre, Toronto General Research Institute, University Health Network, Toronto, ON, Canada

² Department of Biochemistry, Schulich School of Medicine and Dentistry, University of Western Ontario, N6A 5C1

³ Department of Computer Science, University of Western Ontario, N6A 3K7

⁴ Department of Immunology, University of Toronto, Toronto, ON, M5S 1A8, Canada

⁵ Department of Laboratory Medicine and Pathobiology, University of Toronto, Toronto, M5G 1L7, Canada

⁶ Division of Gastroenterology, Hepatology and Nutrition, The Hospital for Sick Children, Toronto, M5G 1X8, Canada

⁷ Toronto Centre for Liver Disease, University Health Network, Toronto, Ontario, Canada.

⁸ Institute of Health Policy, Management and Evaluation, University of Toronto, M5T 3M6, Toronto, Canada

⁹ The Donnelly Centre, University of Toronto, Toronto, ON, M5S 3E1, Canada

Equal contribution first authors

*** Equal contribution senior authors**

Correspondence to Sonya A. MacParland (s.macparland@utoronto.ca) or Tallulah Andrews (tandrew6@uwo.ca) or Diana Nakib (diana.nakib@mail.utoronto.ca) or Gary D. Bader (gary.bader@utoronto.ca) or Ian D. McGilvray (Ian.Mcgilvray@uhn.ca)

Correspondence Address: MaRS TMDT, Rm 3-302, 101 College St, Toronto, Ontario Canada M5G 2L7 (416) 581-7442.

There are no conflicts of interest to declare that are relevant to this work.

Financial Support Statement:

Funding provided in part through the UHN foundation; through grant number CZF2019-002429 from the Chan Zuckerberg Initiative DAF, an advised fund of Silicon Valley Community Foundation; an early researcher award from the Government of Ontario (ERA19-15-210); funds from the University of Toronto's Medicine by Design initiative, which receives funding from the Canada First Research Excellence Fund (CFREF) to SAM, GDB and IDM; by the NRNB (U.S. National Institutes of Health, grant P41 GM103504) to GDB and by the UHN Foundation. DN has received graduate fellowships from CIHR (CGS-D). CTP has received postdoctoral funds from the Canadian Network on Hepatitis C (CanHepC). CanHepC is funded by a joint initiative of the Canadian Institutes of Health Research (CIHR) (NHC-42832) and the Public Health Agency of Canada (PHAC). CTP received postdoctoral funds from PSC Partners Seeking a Cure Canada which was matched by the UHN foundation. Aspects of this work were performed in collaboration with the Canadian Autoimmunity Standardization Core (CIHR-HUI-159423). This work was funded in part by CIHR grants PJT162298 (IDM) and PJT162098 and HIT168002 (SAM). SAM holds a CRC Tier 2 in Liver Immunobiology.

Author Contributions

S.A.M., G.D.B. and I.D.M designed the study. T.S.L, D.N, X.-Z.M., B.K.G., L.L, and P.L. conducted experiments. E.W., B.A., S.M., A.R., and G.H. recruited and consented patients. E.W. S.M., B.S., G.H.M. and I.D.M harvested the surgical specimen. D.N., C.T.P., L.L., D.C. and S.C, X.-Z.M., and J.M. expedited the processing of the harvested surgical specimens for storage and experiments. C.T. interpreted the histology. T.S.A., D.N., P.L., L.L., S.C., D.C., B.H., A.G., A.G., A.R., G.M.H., S.A.M., G.D.B., and I.D.M. analyzed and interpreted the data. T.S.A, D.N., S.A.M., G.D.B. and I.D.M prepared the manuscript with critical revision from all authors.

All authors reviewed this manuscript.

Data & Code Availability

The NDD liver map data and the spatial transcriptomics data are available for exploration with our interaction shiny tools (see links below). Seurat objects and raw count matrices for all of these data and the PSC sc- and sn-RNA-seq data have been uploaded to CELLxGENE Discover and can be found at: <https://cellxgene.cziscience.com/collections/0c8a364b-97b5-4cc8-a593-23c38c6f0ac5>. CELLxGENE Discover allows users to visually explore patterns of gene expression and corresponding clinical metadata using an interactive interface, including differences between healthy and disease samples. The NDD spatial data is currently available at GSE240429, NDD sc- and sn-RNA-seq raw data and raw count matrices are available at

GSE243977, previously published NDD liver data included in this study can be found at GSE115469 ¹ and GSE185477 ², and incorporated data from Ramachandran et al ⁶ can be found at GSE136103. The PSC spatial data is currently available at GSE245620, and the PSC and PBC sc- and snRNA-seq raw count matrices are available at GSE247128. Scripts used to analyze these data are available on our github: <https://github.com/tallulandrews/LiverMap2.0>.

Healthy Map:

<https://macparlandlab.shinyapps.io/generalmap/>

<https://macparlandlab.shinyapps.io/macrophages/>

<https://macparlandlab.shinyapps.io/lymphocytes/>

<https://macparlandlab.shinyapps.io/endothelial/>

<https://macparlandlab.shinyapps.io/cholangiocytes/>

https://macparlandlab.shinyapps.io/b_cells/

<https://macparlandlab.shinyapps.io/stellate/>

Spatial Healthy:

<https://macparlandlab.shinyapps.io/healthylivermapspatialgui/>

Spatial PSC:

https://macparlandlab.shinyapps.io/shinypsc_spatialappgui/

Abstract: 338 words

Background: Primary sclerosing cholangitis (PSC) is an immune-mediated cholestatic liver disease characterized by bile retention, biliary tree destruction, and progressive fibrosis leading to end stage liver disease and transplantation. There is an unmet need to understand the cellular composition of the PSC liver and how it underlies disease pathogenesis. We generated a comprehensive atlas of the PSC liver in comparison to a primary biliary cholangitis (PBC) and reference healthy liver dataset using multiple multi-omic modalities and functional validation.

Methods: We employed single-cell (sc) RNA-seq (47,156 cells), single-nucleus (sn) RNA-seq (23,000 nuclei) and spatial transcriptomics (1 sample by 10x Visium and 5 samples with multi-region profiling by Nanostring GeoMx Digital Spatial Profiler) to profile the cellular ecosystem in 10 patients with PSC. Transcriptomic profiles were compared to 24 neurologically deceased donor livers (107,542 cells) and spatial transcriptomics controls, 18,240 cells and 20,202 nuclei from 3 patients with PBC, and publicly available scRNA-seq data from 5 uninjured, 2 NAFLD, 2 ALD, and 1 PBC liver samples. Flow cytometry and intracellular cytokine staining was performed to validate PSC-specific differences in immune cell phenotype and function.

Results: PSC explants with cirrhosis of the liver parenchyma and prominent periductal fibrosis contained a population of hepatocytes expressing a cholangiocyte-like phenotype. These hepatocytes were surrounded by diverse immune cell populations, including monocyte-like macrophages, liver-resident and circulating natural killer cells. PSC-associated cholangiocytes, hepatic stellate cells, and endothelial cells expressed chemokine and cytokine transcripts typically involved in immune cell recruitment. As well, expanded CD4⁺ T cells, dendritic cells and neutrophils in the PSC liver expressed the corresponding receptors to these chemokines and cytokines, suggesting potential recruitment. Tissue-resident macrophages, by contrast, were reduced in number and exhibited a dysfunctional and downregulated inflammatory response to LPS and IFN- γ stimulation.

Conclusions: We present a comprehensive atlas of the PSC liver and demonstrate hyper-activation and exhaustion-like phenotypes of myeloid cells and markers of chronic cytokine expression in late-stage PSC lesions. This atlas has the potential to expand our understanding of the cellular complexity of PSC and to inform novel treatment development.

Impact and Implications

Primary sclerosing cholangitis (PSC) is a rare liver disease characterized by chronic inflammation and irreparable damage to the bile ducts resulting in liver failure. Due to a limited understanding of the underlying pathogenesis of disease, there remains a paucity of treatment options. We sequenced healthy and diseased livers to compare the activity, interactions, and localization of immune and non-immune cells. This revealed that hepatocytes lining PSC scar regions are transforming into cholangiocytes, whereas immune cells are accumulating within the scars. Of these cells, macrophages, which typically contribute to tissue repair, were enriched in immunoregulatory genes and demonstrated a lack of responsiveness to stimulation. These cells may be involved in maintaining hepatic inflammation and could be targeted in novel therapeutic drug development.

Journal Pre-proof

Introduction

Recent single-cell atlasing efforts have revealed a broad diversity of parenchymal, progenitor, tissue resident and transient circulating immune cells within the liver¹⁻³. Changes in the frequency and characteristics of these populations have also been observed in atlases of acute liver disease, chronic fibrosis, and hepatic cancers⁴⁻⁶. Understanding the healthy liver by building a comprehensive reference map with an inventory of cells and their respective spatial localization is crucial in elucidating the transcriptomic and phenotypic changes, rare cell types, and cell-cell interactions that underlie disease development^{7,8}.

Primary sclerosing cholangitis (PSC) is an immune-mediated cholestatic liver disease that is characterized by the retention of bile, destruction of the biliary tree and development of fibrosis⁹. Given the rarity of the disease and the timeline from diagnosis to end-stage liver disease, few studies have attempted to map the PSC liver and characterize its cellular landscape. Previous transcriptomic maps of PSC have only considered sorted populations of immune cells^{10,11}. These and other studies assessing PSC and PSC-like murine models that have employed bulk tissue expression have implicated CD4⁺ T cells^{10,12}, neutrophils¹³, dendritic cells¹¹, antibody-producing B cells^{14,15}, and macrophages¹⁶⁻²² in the development of disease. However, the focused scope and low cellular resolution of these studies leave many uncertainties in the pathogenesis and outcome of PSC inflammation, preventing the development of targeted treatments.

We present the first single-cell transcriptomic atlas of PSC, and a primary biliary cholangitis (PBC) comparator group, using 5' single-cell, 3' single-nucleus and spatial transcriptomics, as well as a complementary 100,000 cell reference neurologically deceased healthy donor (NDD) liver map. These maps revealed seven disease-associated cell subtypes including T-cell and NK-cell intermediate states, mast cells, dendritic cells, and neutrophils, as well as extensive disease-specific cell-cell interactions between immune and non-immune liver cells. A subpopulation of hepatocytes identified surrounding fibrotic lesions appeared to have lost their zoned expression and co-expressed cholangiocyte-specific markers, while TREM2⁺ and monocyte-like macrophages were concentrated within fibrotic regions. In experimental validations, these macrophages exhibited suppressed inflammatory potential, which could represent a pathway by which these myeloid cells contribute to immune dysregulation in PSC.

Materials and methods

Human Liver Tissue

Healthy human liver tissue from the caudate lobe was obtained from NDD livers which were acceptable for liver transplantation and without evidence of histopathological liver disease. Samples were collected with institutional ethics approval from the University Health Network, Toronto, Canada (REB# 14-7425-AE). PSC samples were collected from explanted tissue sections (~2 cm³) and /or perfusable caudate lobes at the time of transplantation with institutional ethics approval from the University Health Network (REB# 20-5142). All patient clinical characteristics are shown in **Supplementary Table 1**.

NDD, PSC and PBC Sample Collection and Processing for scRNA-seq & snRNA-seq

Samples from NDD (24), PSC (10) and PBC (3) livers were collected and processed for scRNA-seq fresh or following cryopreservation (**Supplementary Table 1**) with a collagenase dissociation protocol ^{1,23} (dx.doi.org/10.17504/protocols.io.m9sc96e), in addition to being snap frozen for snRNA-seq, as previously described, by snap-freezing in liquid nitrogen ^{24,25}, respectively (dx.doi.org/10.17504/protocols.io.261ge34qdl47/v1) (**Figure 1A-B**). Within 1 hour of caudate removal from the donor organ, intact caudate and explanted tissue sections were snap frozen, embedded in optimal cutting temperature (OCT) medium to be stored at -80°C ²⁴, and formalin-fixed and paraffin-embedded (FFPE) for histology, immunohistochemistry (IHC) and immunofluorescence (IF). Remaining total liver homogenate (TLH) was cryopreserved in 90% FBS and 10% DMSO in liquid nitrogen for further experimentation and scRNA-seq. Nuclei for snRNA-seq were extracted from snap frozen tissue, as described previously ^{2,25}.

Preprocessing of 10x Chromium Samples

Sequencing reads were quantified using cellranger mapping to hg18 (for specific versions see **Supplementary Table 1**). Droplets containing viable cells were identified using EmptyDrops from the DropletUtils (v1.2.0) package ²⁶ (**Figure 1A**). Since cell type-specific enrichment and/or sorting prior to loading cells into the 10X Chromium was not performed, identification of viable cells from cellular debris and ambient RNA was performed computationally. EmptyDrops was used with the following parameters: lower=20,000, niters=100,000, ignore=10, retain=100. Viable cells were defined using a 1% FDR threshold.

ScRNA-seq and snRNA-seq Quality Control

To ensure consistent quality across all samples, scRNA-seq data were further filtered with the following criteria: cells were defined as > 500 genes detected, > 875 total unique molecular identifiers (UMIs), and < 50% mitochondrial RNA. The 50% mitochondrial RNA threshold was applied for the liver due to the presence of cells (i.e: hepatocytes) with naturally high mitochondrial counts ¹. Cells from all samples were library-size normalized to 1500 UMIs/cell and log transformed using a pseudocount of 1. Each sample was scaled individually, and the top 2,000 most highly variable genes (HVGs) were identified in each sample using Seurat (v3.1.3) ²⁷. Genes located in the mitochondrial genome were excluded from the set of HVGs,

and cells in each sample were assigned to cell-cycle stages using Seurat's default parameters. Cells were initially annotated using a custom algorithm (see supplementary methods) using our previous map ¹.

Data Integration

Raw, normalized and scaled expression matrices for all samples were merged. Consensus of HVGs were defined as those genes determined to be highly variable in at least two samples and detected in all samples. The samples were integrated using Harmony (v1.0) ²⁸, with default parameters, based on the expression of the consensus highly variable genes. Uniform manifold approximation and projection (UMAPs) were recalculated using the integrated lower dimensional space.

Clustering and Annotation

The integrated NDD liver map was clustered using Seurat (v3.1.3) ²⁷. The resolution parameter and k of the knn graph were varied from 0.3 to 2 and 40 to 80, respectively. The resulting clusterings were defined using apcluster (v1.4.8) ²⁹, with "p" = -2.5, using the variation of information distance metric ³⁰. This resulted in three exemplar clusters, which were compared using the uniformity of the automatic cell-type annotation of each sample to identify the optimal clustering: res = 0.6, k = 50. The resulting clusters were manually annotated by comparing markers of each cluster from the FindMarkers function in Seurat with known cell type specific genes (**Supplementary Table 2 & 3**).

The integrated PSC, PBC and NDD 5' single-cell data were clustered using the top 30 principal components, k=20, res=2 and the integrated PSC, PBC and NDD 3' single-nucleus data were clustered using the top 30 PCs, k=20, res=2. The resolution was increased in order to separate neutrophils from other myeloid populations. Clusters that represented the same cell types were merged during manual annotation (**Supplementary Table 6-7**).

Liver Map Subclustering

The integrated NDD liver map clusters were classified into 8 general classes (**Extended Data Fig. 1**). Cells in each of these classes were subset and subclustered by repeating the entire clustering and integration pipeline (**Extended Data Fig. 2 - 5**). The subclusters were manually annotated using genes significantly highly expressed in that cluster compared to all other clusters ("marker genes") identified using the Wilcoxon-rank-sum test.

Macrophage-Endothelial Cell-Cell Communication Analysis

We used scmap ³¹ to determine the specific identity of macrophages and endothelial cells comprising the macrophage-endothelial doublets (**Extended Data Fig. 6**). Doublets were independently mapped to the macrophage subpopulations and endothelial subpopulations using the most specific marker genes for each cell population as identified during manual annotation

(**Supplementary Table 2**). Only doublets that could be reliably assigned (similarity > 0.6 and consistent between Pearson and Spearman correlations) to a macrophage and endothelial subpopulation were used to determine the number of doublets containing each possible pair of subtypes. Potential ligand-receptor interactions were identified using CellPhoneDB (v4.1.0) ³².

Visium Computational Analysis

Visium spatial transcriptomic data was collected for 1 sample of NDD and 1 sample of PSC liver. Reads were mapped to the Human genome (GRCh38-2020-A), demultiplexed and quantified according to UMIs using spaceranger (v1.1.0). Mitochondrial genome transcripts and genes with no more than 2 UMIs in any spot in the entire tissue slice were removed. Gene expression was normalized using sctransform, and data visualized using Seurat (v4.0.2) ²⁷. Transcriptomic data were clustered using the standard Seurat pipeline: highly variable gene detection, PCA, k-nearest-neighbor detection, Louvain clustering, and wilcoxon-rank-sum test for marker genes, using default parameters. Note, spatially variable genes largely overlapped with highly variable genes but excluded many B cell and red blood cell markers. Zonation scores were calculated by first rotating principal components using the base R varimax function to improve their interpretability (See Supplementary Methods). Protein validations for spatial transcriptomics were performed via IF (**Extended Data Fig. 8**). Significance of zonation was calculated using linear regression between zonation score and the normalized gene expression. Colocalization was determined using Pearson correlation.

Pathway Analysis

Genes were ranked by their estimated fold changes. Pathway analysis was performed using gene set enrichment analysis as implemented in the fgsea package (v1.8.0) with 5% FDR and 100,000 permutations using the MSigdb Hallmark pathways, MSigdb Immune pathways, and Reactome pathways. Only terms including between 15 and 1000 annotated genes were considered. Pathways detected at a 5% FDR were reported as significant. The Jaccard index was calculated between genes associated with each pair of enriched pathways and used to manually collapse redundant pathways from each annotation source.

Cell-Type Comparisons of PSC or PBC vs. NDD

To compare cell type specific differential expression between PSC and NDD single-cell and single-nucleus data, we calculated pseudobulk gene expression for each cell type in each sample by summing the respective raw UMI counts. Pseudobulks were compared between NDD and PSC/PBC using edgeR's exactTest ³³ using only genes passing QC thresholds in PSC, PBC and NDD data and cell types with at least 2 samples in each condition containing at least 10 cells of that type (**Supplementary Table 4 & 5**). Differentially expressed genes were identified using FDR < 0.05. Pathway enrichments were calculated as above and cell-cell interactions were identified using ligand-receptor interactions obtained from the KEGG Cytokine pathway (hsa04060). Note, we only consider Cytokine pathways to avoid these pathways being obfuscated by adhesion and complement cascade pathways that are very common between our hepatocyte and endothelial cells.

Cell type frequencies were calculated for each sample, and differences between NDD and PSC were determined using the Wilcoxon rank-sum test. Of note, there were too few samples of PBC (N=2) to accurately estimate sample-sample heterogeneity in cell-type frequency.

Integration of Publicly Available Cirrhosis scRNA-seq Data

Published liver single-cell RNAseq cirrhosis data were obtained from the original authors⁶. Cell types were reannotated using marker genes and cell type names defined in this manuscript (**Extended Data Fig. 10**). Differential expression and changes in cell type frequencies between cirrhotic and non-cirrhotic (tumor adjacent) tissue was performed, as described above.

In Silico Flow Sorting

To compare our single-cell RNAseq data to our flow cytometry data, we performed *in silico* gating of our single-cell data using thresholds based on the non-immune fraction: PTPRC > 0.3, CD68 > 0.3. PSC scRNA-seq was enriched in immune expression overall compared to NDD, thus higher thresholds for “on” for each gene were determined based on maximum expression seen in non-immune cell types. Tissue was prepared for Visium Spatial transcriptomics as previously described². Briefly, liver tissue was embedded in OCT media, frozen at -80°C, and cryosectioned with 16- μ m thickness at -10°C (cryostar NX70 HOMP). Sections were placed on a chilled Visium Tissue Optimization Slide (10x Genomics) and processed following the Visium Spatial Gene Expression User Guide. Tissue was permeabilized for 12 minutes, based on an initial optimizations trial. Libraries were prepared according to the Visium Spatial Gene Expression User Guide and samples sequenced on a NovaSeq 6000.

10x Genomics Visium Experimental Protocol

Tissue was prepared for Visium Spatial transcriptomics as previously described². Briefly, liver tissue was embedded in OCT media, frozen at -80°C, and cryosectioned with 16- μ m thickness at -10°C (cryostar NX70 HOMP). Sections were placed on a chilled Visium Tissue Optimization Slide (10x Genomics) and processed following the Visium Spatial Gene Expression User Guide. Tissue was permeabilized for 12 minutes, based on an initial optimizations trial. Libraries were prepared according to the Visium Spatial Gene Expression User Guide and samples sequenced on a NovaSeq 6000.

Nanostring GeoMx Digital Spatial Profiling Platform

PSC and NDD liver sections were sliced from OCT-embedded sections and submitted to NanoString for staining with selected morphological markers: DAPI (nuclei), KRT (epithelial cells), CD45 (immune cells), and CD68 (macrophages). For this experiment, we employed the GeoMx Cancer Transcriptome Atlas that contains over 1800 immune- and cancer-related targets. Expression data were deconvolved into cell type composition using Nanostring GeoMx digital spatial profiling software (v3.0.0.113)³⁴ and the marker genes from our NDD liver map (**Supplementary Table 2**).

Flow Cytometry & Cytokine Analysis

Cell suspensions from frozen TLH were stained as previously described^{1,35,36} with live/dead Zombie Violet (Biolegend, 423114) or Zombie NIR (Biolegend, 423106) to assess viable cells and fluorophore-conjugated monoclonal antibodies to the following human cell-surface markers: anti-CD45-BV650 (Biolegend, 304044), anti-CD206-AF647 (Biolegend, 321116), anti-HLADR-AF700 (Biolegend, 307626), anti-CD68-R780 (Biolegend, 333816), and anti-CD68-PeCyp5.5 (Biolegend, 333814). Intracellular cytokine staining (ICS) was performed to examine the functional differences in CD68⁺ cells that were either CD206⁺ or CD206⁻ in PSC, PBC and NDD TLH. Cell suspensions (2x10⁶ cells) from the non-parenchymal cell (NPC) fraction were stimulated in 12-well plates with 10 ng/ml LPS (L2880-10MG), 25ng/ml IFN γ (Thermofisher, PHC4031) for 6 hours in the presence of brefeldin (BD Biosciences, 555029) and monensin (BD Biosciences, 554724). Intracellular secretion of TNF α , detected with anti-TNF α -PeCy7 (Biolegend, 502930) and anti-TNF α -PacBlue (Biolegend, 502920), was examined as previously described^{1,35}. Gating strategy for cell-surface markers was set based on background auto-fluorescence measured in unstained and fluorescence minus one (FMO) controls, and gating strategy for intracellular markers in stimulated samples was set based on unstimulated controls and FMOs. Plots were generated and statistical tests were performed in Prism (v10.1.0).

Histopathology, Immunohistochemistry and Immunofluorescence of FFPE samples

To validate *in silico* findings, FFPE tissue sections were employed for histology, IHC and IF staining. Disease stage was defined by the Nakanuma score and stage³⁷ by assessing the following components, 1) fibrosis, and 2) bile duct loss. Annotation of fibrotic areas and chronic biliary disease, referred to as 'scars' in this study, within the liver parenchyma of PSC explant livers were defined based on Masson's trichrome stain (highlighting fibrosis) and Cytokeratin 7 (CK7) immunohistochemical stain (highlighting biliary metaplasia in hepatocytes as a feature of chronic biliary disease)³⁸. CK7 staining highlights the hepatocytes with biliary metaplasia near the edges of fibrotic areas (scars) in PSC explant samples (**Extended Data Fig. 11, 22-23**). IF was performed through the Pathology Research Program at the University Health Network on NDD, PSC and PBC samples, and scanned by the Advanced Optical Microscopy Facility. Antibodies included anti-VCAM1 (Thermofisher, MA5-11447), anti-CD32 (Thermofisher, MA5-32601), anti-C1QC (Abcam, ab75756), anti-CK7 (Abcam, ab68459), anti-HNF4A (Abcam, ab41898), anti-CD9 (Abcam, ab236630), and anti-CD36 (ab17044). Analysis of IF experiments and liver immune cell detection was performed on QuPath (v0.4.3), as previously described³⁹ ([dx.doi.org/10.17504/protocols.io.bs6gnhbw](https://doi.org/10.17504/protocols.io.bs6gnhbw)), and plots were generated and statistical tests were performed in Prism (v10.1.0).

Results

Global NDD Liver Map

To generate an expanded reference single-cell liver atlas suitable for identifying PSC-aberrant transcriptomic patterns, we collected single-cell transcriptomes from over 100,000 single cells from 24 different NDD livers with equal representation of males and females spanning a wide age range (**Figure 1**). ScRNA-seq was generated using the 10x Chromium with both 3' and 5'

chemistries (**Supplementary Table 1, Figure 1 C**). Samples were integrated into a single atlas, which was clustered into 20 coarse-level cell groups. We found that all samples merged together and contributed to almost every cell cluster in our map and that cellular phenotypes were remarkably consistent across demographic factors (Pearson correlation between donors > 0.5 in 17/20 clusters) (**Figure 1 G, Supplementary Table 3**). Using compositional analysis (see Methods), we found significant variations in cell type frequencies across samples (**Figure 1 F**). However, this is likely due to dissociation and tissue sampling effects rather than donor-specific differences, as significant associations between cell type frequency and donor sex or age were not identified (linear regression Benjamini-Hochberg adjusted p-value > 0.3). These coarse level cell types were subclustered into a final total of 38 cell states (**Extended Data Fig. 2-5**). These included tissue-resident and circulating NK cells, naive and plasma B-cells, and an ultra-rare population of mucus-producing cholangiocytes.

Expanded NDD liver map elucidates human macrophage diversity

Our original liver atlas, based on five NDD livers, was able to distinguish two different macrophage populations characterized by opposing relationships with inflammation¹. However, a larger diversity of macrophages has been observed in disease datasets^{6,3}. To determine if these macrophage subtypes were present in non-diseased NDD livers, we subclustered our macrophage populations. Subclustering revealed additional macrophage diversity among the 11,127 macrophages of our expanded map (**Figure 2 A**). We identified 15 subclusters among the macrophages in our map, several of which exhibited simply different expression in inflammatory (S100A8, S100A9, S100A6, VCAN, LYZ) or known non-inflammatory (CD5L, MARCO, VCAM1) markers. These clusters were merged together due to their lack of unique marker genes, leaving 10 distinct phenotypes of macrophages that were both conserved across donors and consistent with the macrophage subtypes identified in Guilliams et al.³ (**Extended Data Fig. 5**). After merging, non-inflammatory Kupffer cells and inflammatory monocyte-derived macrophages accounted for 40% of all macrophages in the NDD liver.

The remaining 60% were spread across 8 rarer phenotypes, including LYVE1⁺ FOLR2⁺ TIMD4⁺ non-inflammatory resident macrophages and VSIG4⁺ macrophages. The former population was similar to the self-renewing resident cardiac macrophages found in mice^{40,41} and were found in 23/24 NDD livers, but were not distinguishable from Kupffer cells in diseased livers. Whereas, MHCII^{high} VSIG4⁺ macrophages were similar to those observed in many mouse tissues⁴², and were found in 23/24 NDD livers and all PSC/PBC livers, as well as in published NAFLD/ALD liver data (**Figure 2, Extended Data Fig. 10**).

In addition, we identified a novel macrophage subtype characterized by the expression of PLAC8, LST1, IFITM3, AIF1 and COTL1 genes, in addition to some inflammatory markers (FCN1, LYZ, S100A4, S100A8). This population was found in 23/24 NDD livers but was not distinguishable in PSC/PBC livers. COTL1 and LST1 are cytoskeleton-related proteins involved in lamellipodia at immune synapses^{43,44}. CD52, another top marker of this cluster, is involved in interactions with T cells⁴⁵. Pathway enrichment analysis revealed an upregulation pathways relating to the interferon-alpha (IFN α) response, TCR signaling, immunological synapses and

IL8-CXCR2 signaling (**Figure 2 B**). These results suggest that these inflammatory macrophages are specialized in interacting with T cells.

The rarest subtype of macrophages (5%) uniquely expressed CD9, GPNMB, TREM2, FABP5, ACP5, PLD3 and LGMN, similar to previously described 'lipid-associated' macrophages (LAM-like) and cirrhosis scar-associated macrophages^{3,6,46}. This population was found in 22/24 NDD donors and all PSC/PBC livers where scRNA-seq data were collected, and expression of CD9 protein was validated by IF (**Extended Data Fig. 6 D**). Pathway analysis revealed an enrichment of pathways related to the phagosome and lysosome (**Figure 2 B**).

In addition to these subtypes of macrophages, we observed a type-independent activation pathway in macrophages. This signature was characterized by high expression of IL1B, CD83, CXCL2, CXCL3, NAMPT, THBS1, and AREG, as well as genes involved in pathways associated with *in vitro* LPS stimulation of macrophages and TNF α signaling (**Figure 2 B**). This pathway was observed in both monocyte-like macrophages and macrophages lacking any other phenotype-signature. This population was found in 20/24 NDD livers, as well as all PSC/PBC livers (PBC samples having twice the number of activated macrophages than PSC samples) but was not observed in NAFLD/ALD livers.

Examination of cell-cell communication suggests endothelial cells may be involved in the recruitment of myeloid cells in PSC

Previous work has shown that liver sinusoidal endothelial cells (LSECs) are important in recruiting monocytes to the liver after injury. LSECs have been shown to contribute to inducing a Kupffer cell-like phenotype in recruited monocytes upon artificial depletion of native Kupffer cells in mouse models^{47,48}. Interestingly, we found a significant number of doublets between macrophages and LSECs in our NDD human liver that expressed macrophage markers (CD163, CD68, TIMP1, and C1q) and LSEC markers (DNASE1L3, ENG, SPARC, CLEC1B). These doublet cells accounted for 282 cells (3% of all macrophages), which was 10-fold higher than we expected based on the loading of our samples and frequency of macrophages and LSECs in our map (expect: 0.3%, $p < 10^{-100}$). Using scmap³¹, 142/282 doublets were reliably assigned to both a specific macrophage subcluster and a specific endothelial subcluster (**Figure 2 E**). Of these, the most common pairwise interaction was between Kupffer cells and central venous LSECs (cvLSECs). These doublets were also observed in small numbers in PSC samples (**Figure 3A**). Immunofluorescent staining confirmed the co-localization of endothelial (CD36) and Kupffer (C1QC) cells at the protein level in the NDD liver (**Figure 2F**).

However, monocyte-like macrophages were specifically enriched in doublets with central venous endothelial cells (cvEndo) that line the central vein. To confirm that these doublets represent cell-cell interactions, we used CellPhoneDB³². Results were filtered to identify interacting proteins involved in cell-cell adherence or close-contact cell-cell communication that were specific to cvEndo and monocyte-like macrophages (**Extended Data Fig. 6A,B, Figure 2E**). The 10 top interactions after filtering included SELL-PODXL, which is involved in immune cell rolling-adhesion⁴⁹, ITGAL/SPN-ICAM1, which is important for tissue infiltration of immune

cells⁵⁰, and SELP-SELPG, a mediator of leukocyte recruitment⁵¹ (**Extended Data Fig 6B**). These results indicate a potential recruitment pathway for monocytes from the blood binding to endothelial cells in the central vein and being recruited into the liver.

Spatial transcriptomics identifies spatial location of macrophage populations.

To add a spatial dimension to our single-cell atlas, we sequenced four consecutive z-stack slices using 10x Genomics VISIUM spatial transcriptomics (**Figure 2 C,D, Extended Data Fig. 7**). Hepatocyte zonation was captured as either the first or second principal component in each slice. This score was used as a weight to calculate the average zonation of individual genes, which were summed across cell-type markers to determine the average enrichment of specific cell types. These results confirmed our endothelial cell annotations, and indicated that NK, T and B cells were weakly periportal (**Extended Data Fig. 7 E-F**). Examining macrophage subsets, we found that MHCII⁺, LAM-like macrophages and Kupffer cells were slightly pericentral, while activated macrophages were periportal (**Figure 2 D**). IF validation revealed a bimodal distribution of VCAM1⁺ cells, i.e. putative Kupffer cells, with increased frequency in both the periportal and pericentral region; however, only the increase in periportal regions reached statistical significance (**Extended Data Fig. 8**).

Cholangiocyte-like hepatocytes are enriched in liver disease

We collected 5' scRNA-seq (**Figure 3**) and 3' snRNA-seq (**Figure 4**) data from explanted livers from 10 patients with PSC and 3 patients with primary biliary cholangitis PBC. To provide a NDD reference for our 3' snRNA-seq data from PSC and PBC livers, we combined 24,511 single nuclei from 4 NDD livers from our previously published NDD map² with 53,284 nuclei from 7 PSC livers, and 20,202 nuclei from 2 PBC livers. As we observed previously, immune cell populations were poorly captured with snRNA-seq but large numbers of hepatocytes, cholangiocytes, and endothelial cells were observed (**Figure 3A**). In comparison to NDD livers, PBC and PSC samples contained fewer periportal hepatocytes (P-Hepato2, 70% loss, $p=0.02$), a greater number of activated stellate cells (aStellate 3-fold increase, $p = 0.04$), and a greater number of cholangiocytes (2.5-fold increase, $p = 0.3$) (**Figure 3C**). Interestingly, we found that interzonal hepatocytes (I-Hepato), hepatocytes that lack pericentral and periportal markers, were significantly increased in PSC and PBC (2.3-fold increase, $p = 0.04$). These hepatocytes upregulate many genes involved in immunological pathways, such as TNF α signaling, IFN γ response, and allograft rejection, as well as pathways involved in dedifferentiation, such as KRAS and epithelial-mesenchymal transition signaling (**Extended Data Fig. 9**). In particular, many cholangiocyte-related genes, including KRT7, BICC1, FGF13, and DCDC2, were upregulated in both PBC and PSC in this hepatocyte population compared to NDD controls (**Figure 3B**). In contrast, classical hepatocyte markers, including ALB, CYP3A4, and APOA1, were downregulated. We identified a similar pattern in published scRNA-seq datasets⁶ which compared alcoholic liver disease (ALD) and non-alcoholic fatty liver disease (NAFLD) to uninjured liver (**Extended Data Fig. 10E**). These findings suggest that a shift towards a cholangiocyte-like phenotype is a common feature of disease-associated hepatocytes across many forms of liver cirrhosis. We directly observed this phenomenon in our PSC livers by IF

using HNF4A as a marker of hepatocytes and CK7 as a marker of cholangiocytes. We observed a decrease in HNF4A, an increase in CK7 and an increase in co-expression of the markers in PSC compared to NDD livers (**Figure 3 D,E, Extended Data Fig 11**). This was consistent with the hepatocyte metaplasia observed during disease-scoring of these samples (**Extended Data Fig 22,23**).

Immune expansion identified within scar regions

We created a combined 5' scRNA-seq map from 24,007 cells from 6 livers of our NDD map that were sequenced using 5' technology, 44,150 cells from 8 PSC livers, and 17,230 cells from 2 PBC livers (**Figure 4A**). We excluded 3' scRNA-seq NDD samples to avoid biasing comparisons with 5' scRNA-seq diseased livers. While hepatocytes, stellate cells and cholangiocytes are well represented in the single-nucleus map, lymphocyte populations were difficult to distinguish. In contrast, our single-cell map revealed the presence of both plasmacytoid and conventional dendritic cells, and a large diversity of lymphocyte populations, including many that were not present in our NDD map (**Figure 4 A, Extended Data Fig 12 B,D**). Similar to what has previously been described in fibrotic livers⁵², we observed increases in disease-specific lymphocyte populations including two distinct populations of NK T-like cells (**Extended Data Fig. 12 D**), one that expressed liver resident NK cell (lrNK) markers (EOMES, CMC1, KLRC1, KLRF1, XCL1)⁵³ and CD3⁺ T cell markers (CD3D, CD3E, TRAC, TRBC2), as well as another population that expressed circulating NK cell (cNK) markers (FCGR3A, GNLY, GZMK, TBX21, XCL2)⁵⁴ and CD8⁺ T cell markers (CD8A, CD8B, CD3D, CD3E). DoubletFinder² determined that these populations are not doublets (estimated 3% doublets for CD3T-lrNK, 10% for CD8T-cNK). These populations were predominantly found in PBC (965 cells, 6%) and PSC (2879 cells, 6%), but not found in the NDD livers (<100 cells, 0.2%) nor the published ALD/NAFLD data⁶. Comparing these populations to the most similar NK and T cells, we found that the CD8T-cNK population downregulated pro-inflammatory CCL3⁵⁵ (log2FC -0.4, $p < 10^{-10}$) and upregulated anti-inflammatory KLF2⁵⁶ (log2FC 0.5, $p < 10^{-100}$). In contrast, the CD3T-lrNK population upregulated pro-inflammatory cytokines CCL5 (log2FC 0.75, $p < 10^{-100}$) and IL23 (log2FC 0.39, $p < 10^{-50}$), as well as TRDV1 and TRGV3, suggesting these may be gdT cells.

Differential expression between PSC and NDD livers revealed significant upregulation of many inflammatory pathways including: IL12, IL23, IL27, IFN γ and TNF α pathways in Kupffer cells, T and NK cells, and TNF α , IFN γ , IL2, KRAS and epithelial-mesenchymal transition pathways in hepatocytes, cholangiocytes, and hepatic stellate cells (**Figure 4B**). Most of these pathways were also observed upregulated in PBC, but the upregulation of IL12 signaling in Kupffer cells and NK cells was only seen in PSC. Moreover, PSC-derived NK cells expressed more genes involved in the IFN γ response than PBC (**Extended Data Fig. 13**).

To examine inflammation-related cell-cell signaling, we examined the expression of gene pairs from the KEGG cytokine pathway (hsa04060). We found evidence of interactions between CCR7⁺ CD4⁺ T cells and CCL19⁺ stellate or CCL21⁺ ppLSEC cells in fibrotic regions in PSC and PBC (**Figure 4 C**). The colocalization of CCL19, CCL21 and IL7R (CD4⁺ T cells) was confirmed in our VISIUM spatial transcriptomics data (Pearson correlation 0.2, $p < 10^{-30}$, **Figure 4 D**),

and across multiple replicates of spatial transcriptomics using the Nanostring GeoMx digital spatial profiling platform (**Figure 5 C-D, Extended Data Fig. 14**). Using Nanostring, we observed the colocalization of CD4⁺ T cells, stellate cells, ppLSECs and mature B cells in PSC. However, this was only the case for the examined advanced diseased regions. Large-scale heterogeneity was observed between different regions of interest from the same original liver samples.

Macrophage dysfunction in PSC livers

Unlike the lymphocyte populations, which upregulate inflammatory pathways in PSC, macrophages exhibit increased expression of inhibitory signaling molecules in PSC, including KLF2⁵⁶, OTULINL, and IL27RA. IL27RA has been shown to suppress cytokine production in macrophages^{57,58} and is upregulated in PSC Kupffer cells (log₂FC 2.1, FDR 0.03), and in both PSC and PBC LAM-like macrophages (log₂FC 2.3, FDR 0.001). OTULINL is a potent negative regulator of macrophage activation, and deficiency causes autoimmune disease that can be rescued with anti-TNF therapy⁵⁹. We observed significant upregulation of OTULINL in all macrophage populations in PSC and PBC livers (log₂FC 3.4-5.4, FDR < 0.001). Monocyte-like macrophages adopted a fibrosis-associated phenotype with the upregulation of LGALS3, SPP1⁶ and ADA2⁶⁰; of these, only ADA2 was upregulated in PBC monocyte-like macrophages. In addition, we observed that TGF- β , a potent suppressor of macrophage function⁶¹, co-localized with these cells within those regions (**Extended Data Fig. 15**). We confirmed this scar-associated phenotype of monocyte-like macrophages using our spatial transcriptomics data, which indicates an enrichment of these cells around cholangiocytes in the center of fibrotic regions containing concentric periductal fibrosis (**Figure 5A,B, Extended Data Fig. 14**), whereas, Kupffer cells were localized outside of the scar regions (**Extended Data Fig. 15 D**).

Subclustering of our scRNA-seq map revealed greater macrophage diversity among PSC macrophages (**Extended Data Fig 16A**) with 25 clusters containing at least 50 cells derived from PSC samples vs. 13 clusters from PBC and only 7 clusters from NDD macrophages. Furthermore, we consider 9 of the clusters as PSC-enriched as > 90% of the cells within the cluster originated from PSC livers (**Extended Data Fig. 16B**). In contrast, we observed no PBC-specific cluster; all 13 clusters containing significant numbers of PBC cells also included at least 30% PSC cells. The PSC-specific clusters were predominantly monocyte-like (5/9), whereas macrophages shared between PBC and PSC included 4/13 clusters expressing Kupffer cell markers (MARCO, CD5L, VCAM1) and 2/13 highly expressing MHCII components. Using pathway analysis of the marker genes of each of these subclusters (**Extended Data Fig. 16E**), we identified downregulation of 'interferon signaling' in 7/9 PSC-specific clusters and 2/7 clusters shared between PSC and NDD, but only 1/13 clusters containing PBC cells. Similarly, MHCII presentation was only downregulated in the PSC-specific clusters (3/9) but upregulated in clusters shared with PBC (1/13) and NDD clusters (2/7).

Flow cytometry of primary patient macrophages revealed a significant depletion of CD68⁺ cells relative to CD45⁺ (PTPRC) cells in PSC, which was confirmed with *in silico* gating of our single-cell data (**Figure 6 A-C, Extended Data Fig. 17 - 20**). Additionally, as previously described in

PSC²⁰, we observed increased percentages of CD206⁺ macrophages in PSC in comparison to NDD (**Figure 6 D-E**). Intracellular cytokine staining (ICS) stimulation assays indicated a significantly reduced capacity of PSC macrophages to secrete TNF α in response to LPS and IFN γ stimulation, in comparison to NDD and PBC macrophages (**Figure 6 F-G**). However, when we exposed NDD-derived myeloid populations to recombinant TGF- β (**Extended Data Fig. 21**), we did not observe blunted LPS responsiveness in the CD206⁺ HLA-DR⁺ population.

Discussion

A major challenge in understanding the cellular ecosystem of PSC is the lack of comprehensive maps of the parenchymal and non-parenchymal cells in the PSC liver with single cell resolution. Previous transcriptomic studies of the cellular landscape of PSC have employed bulk RNA-seq on liver tissue^{12,13,18,62} and/or scRNA-seq on sorted immune cell populations¹⁰ and have uncovered important aspects of the immunobiology of PSC. Namely, these studies have identified the potential involvement of TH17 cells and B cells in PSC pathogenesis^{10,14,15,21}, as well as uncovering distinct ductular and fibrosis-associated signatures^{18,62}. Taken together, these works imply that there is a complex cellular interplay driving PSC disease, providing a rationale for our in-depth examination of parenchymal and non-parenchymal cell populations in the PSC liver.

Our multimodal study centered on linking transcriptomic signatures to spatial positioning and functional validation. Specifically, transitioning cholangiocyte-like hepatocytes were identified in both sc- and snRNA-seq, as well as spatial transcriptomics, wherein the transdifferentiating population was shown to localize around the perimeter of PSC scars. Through IF, we observed that this population is significantly enriched in the PSC liver. Additionally, spatial transcriptomics revealed the distinct and exclusive localization of inflammatory and non-inflammatory myeloid populations in relation to PSC scars, and demonstrated the presence of expanded immune populations within these scars, corroborating the increased immunological diversity shown by scRNA-seq. We observed the enrichment of immunosuppressive transcripts in PSC-specific monocytes but an expansion of activated macrophages in PBC, which is reflected in functional validation experiments demonstrating dysfunction in PSC myeloid populations. Beyond understanding the cellular identities in the PSC niche, we also examined cellular locations as a means to better link cell states to the degree of histological damage in the liver. Previously, Chung et al.⁵² found distinct fibrosis-enriched immune populations, a finding that we further refined with the deconvolution of 10x Visium data with our PSC scRNA-seq map. This is supplemented by our examination of the linkage between the heterogeneity of disease through the deconvolution of Nanostring GeoMx DSP data, which revealed the enrichment of immune populations in progressed fibrosis.

In the NDD liver, we uncovered 38 distinct cell types and cell states including a pericentrally located myeloid population similar to the previously described lipid-associated macrophages^{3,46}, as well as myeloid subpopulations associated with immunological synapses and a consistent activation signature (**Figure 2**). In the PSC liver, we identified a further 7 disease-associated cellular states including NKT-like cells, neutrophils, dendritic cells, and a subpopulation of

hepatocytes (**Figure 3-4, Supplementary Table 6**). These immune populations are likely a result of *in situ* expansion and recruitment from the blood into the diseased liver tissue^{11,13,15}. As previously reported for healthy liver tissue, immune subpopulations could only be identified in scRNA-seq (**Supplementary Table 7**), whereas the hepatocyte subtype was only detected in snRNA-seq (**Supplementary Table 8**)². Many of the immune populations were colocalized within fibrotic ‘scar’ regions in PSC, including CD4⁺ T cells and antibody-secreting B cells, which is consistent with bulk RNAseq findings of enrichment of B lymphocytes and FOXP3⁺CD4⁺ T cells in the PSC liver⁶³

In contrast, we observed that disease-associated hepatocytes were specifically located in the border regions surrounding the fibrotic ‘scar’ regions in PSC (**Figure 3, Extended Data Fig. 22 & 23**). These hepatocytes expressed many markers associated with cholangiocytes suggesting they may be transforming into cholangiocytes. Previous studies have demonstrated hepatocytes undergo this transition in the absence of functional bile ducts in a TGF- β -mediated manner^{64,65}. Consistent with these results, TGF- β was expressed in the PSC fibrotic regions, particularly in scars with transitioning hepatocyte edges (**Extended Data Fig. 13**).

We examined the functional capacity of CD206⁺ myeloid cells in PSC and observed suppressed TNF α cytokine secretion and reduced inflammatory potential by CD206⁺ KC-like myeloid cells following stimulation (**Figure 6**). A similar cytokine secretion dysfunction has been reported in inflammatory bowel disease (IBD), a common comorbidity of PSC^{66,67}. This suggests a possible mechanism by which macrophage dysfunction may underlie PSC and IBD pathogenesis^{13,16,20}. We examined the impact of TGF- β incubation on NDD-derived myeloid populations (**Extended Data Fig. 21**) and could not recapitulate the hyporesponsiveness of CD206⁺ and HLA-DR⁺ macrophages in PSC. This further reinforces the complex and multifactorial pathogenesis of PSC, given that spatial transcriptomic signatures demonstrate significant immune recruitment to the PSC scars, such as plasma B cells, inflammatory macrophages and T cells. This demonstrates the importance of future work to focus on early stage disease to identify early actors in PSC development.

Like most studies on PSC^{10,11,18}, much of our data is limited to a single region of each end-stage explanted liver, which was compared to non-diseased livers. However, additional non-PSC disease datasets will serve to further refine these findings. Given the slow progressive nature of PSC development, it remains to be determined whether the findings we report here are PSC-specific and occur during disease pathogenesis, or whether they represent general features of late-stage cholestatic liver disease. In addition, our Nanostring spatial transcriptomic data revealed substantial heterogeneity in disease phenotype across relatively small regions of these livers (**Figure 5**). Thus, future work will expand this map to recover temporal and spatial heterogeneity of disease. Our results demonstrate the power of combining multiple high-resolution gene expression platforms including 3’ single cell, 5’ single cell, single nucleus and spatial transcriptomics to fully elucidate the interactions between the tissue microenvironment, cellular identity, and immunological function underlying a complex inflammatory disease. Taken together, this atlasing effort provides a framework for investigating the drivers of PSC and uncovering precision medicine targets for immunomodulatory and cell-based therapies.

Abbreviations

AntiB = antibody secreting B cells, also known as Plasma cells, that express CD79A, CD79B and various light and heavy chains of the B cell receptor (probably as soluble antibodies) e.g.

IGKC, IGHG, IGLC, IGHA1/2

ALD = Alcoholic liver disease

BCR = B cell receptor

CD45 = cluster of differentiation antigen 45, originally called leukocyte common antigen, the protein produced by the PTPRC gene in humans.

CD206 = the protein produced by the MRC1 gene, a marker of tissue resident macrophages

cvEndo = central venous endothelial cells

DMSO = dimethyl sulfoxide

CK7 = the protein produced by KRT7 gene

FBS = fetal bovine serum

FDR = false discovery rate

FFPE = formalin-fixed and paraffin-embedded

FMO = fluorescence minus one

HVG = highly variable genes

IBD = inflammatory bowel disease

ICS = Intracellular cytokine staining

ICU = Intensive care unit

IF = immunofluorescence

IFN γ = Interferon gamma

IHC = immunohistochemistry

KC = kupffer cells

LAM = lipid associated macrophage

LPS = Lipopolysaccharides

LSEC = liver sinusoidal endothelial cells

ppLSEC = periportal liver sinusoidal endothelial cells

cvLSEC = central venous liver sinusoidal endothelial cells

MHCII = MHC Class II molecules, a class of major histocompatibility complex (MHC), includes HLA-DRA, HLA-DPA1, HLA-DQB1, HLA-DPB1.

NDD = neurologically deceased donor

NAFLD = Nonalcoholic fatty liver disease

NK cells = natural killer cells

cNK = circulating natural killer cells

lrNK = liver resident natural killer cells

NKT = natural killer T cells

NPC = non-parenchymal cell

PSC = Primary sclerosing cholangitis

PBC = Primary biliary cholangitis

QC: quality control

scRNA-seq = single-cell RNA sequencing

snRNA-seq = single-nucleus RNA sequencing
 ST = spatial transcriptomics
 TLH = Total liver homogenate
 TNF α = Tumor necrosis factor alpha
 TGF β = Transforming growth factor beta
 UMAP: Uniform manifold approximation and projection
 UMI = unique molecular identifier

All other abbreviations are official HGNC gene symbols.

Figure Captions

Figure 1: 100k single-cell map of NDD Human Liver reveals conserved cell-types across donors. (A) Single-cell RNAseq sample collection and analysis workflow (B) Table of samples sequenced in this study. (C) Integrated UMAP, containing 20 clusters annotated to 15 major cell-types (D) Age and sex profiles of the 24 donor livers pink = female, blue = male. (E) Proportion of cells from different technologies, sexes and ages contributing to each cell-type of the integrated data. Black points indicate significant enrichment / depletion ($p < 0.05$) based on a hypergeometric test using compositional analysis. There were no significant associations between demographic characteristics and the frequency of different cell-types. (G) Average correlation of the cluster profiles between different donors. The cluster profile is the mean expression of cells within that cluster. Dashed line indicates the average correlation between the cluster profiles of different clusters within the same donor.

Figure 2: Macrophage diversity revealed by expanded NDD Liver map. (A) 11,127 macrophages were subclustered using Seurat and manually annotated to identify 10 distinct phenotypes. (B) Each subtype was enriched for distinct functional pathways as determined by GSEA. (C) Varimax PCA identifies a component that quantifies the zonation of each spot. Black hexagons indicate pericentral veins of distinct lobules. (D) Using the zonation score across four slices of spatial transcriptomics, we determine non-inflammatory macrophage populations are pericentral while activated macrophages are periportal. (E) Number of doublets assigned to each specific pair of subtypes using scmap. (F) Immunofluorescence of LSEC marker CD36 (red) and Kupffer cell marker C1QC (green) confirms presence of colocalized LSECs and Kupffer cells. (G) Percentage of cells over total cells that are co-expressing CD36⁺C1QC⁺, single positive CD36, and single positive C1QC.

Figure 3: Hepatocyte transdifferentiation in biliary disease. (A) Integrated map of 24,511 NDD nuclei, 53,284 PSC nuclei, and 20,202 PBC nuclei. (B) Expression of hepatocyte and cholangiocyte markers across hepatocytes and cholangiocyte subtypes. (C) Frequency of each cell-type among livers of each aetiology, significance obtained from Wilcoxon rank sum test across sample: * p value < 0.05 , ** p value < 0.01 , *** p value < 0.001 (i) rare cell-types making up less than 1% of the total map. (ii) cell-types making up $> 1\%$ of the total map. (D) Representative IF image of a periportal (PP) region in the PSC liver. (E) Quantification of (i) CK7, (ii) HNF4A⁺, (iii) double CK7⁺HNF4A⁺ positive cells, significance obtained from Mann-

Whitney test across samples: * $P < 0.05$, ** $P < 0.01$, *** $P < 0.001$, **** $P < 0.0001$.

Figure 4: Single-cell RNAseq reveals immunological complexity of PSC & PBC (A)

Integrated map of 44,150 cells from PSC, 17,230 cells from PBC, and 24,007 NDD liver cells into a single map. (B) significantly enriched pathways obtained from gene set enrichment analysis (GSEA) on genes differentially expressed between PSC and NDD livers for each cell-type. (C) Expression of ligand-receptor pairs for known cytokines from the KEGG database in PSC, PBC, and NDD cells. Arrows indicate ligand to receptor relationships. (D) VISIUM spatial transcriptomics of key marker genes of immune populations. (i) naive B cells (ii) plasma B cells (iii-iv) CD4⁺T (v-vi) ppLSECs (vii-viii) hepatic stellate cells.

Figure 5: Enrichment of Immune cells in PSC (fibrotic areas) (A)

Visium spatial transcriptomics was clustered and identified layers of distinct regions around fibrotic areas in PSC. (B) Expression of marker genes for each lymphocyte and macrophage subtype from the PSC and NDD single-cell maps in the PSC Visium data. LAMs and Monocytes were enriched in the core of scars near cholangiocytes and periphery of fibrotic areas, while B cells, T cells, and antigen presenting cells were enriched in the center of fibrotic regions, whereas NK cells present at the periphery. (C) Deconvolution of Nanostring digital spatial expression using cell-type markers from the NDD and PSC single-cell maps. (D) Images of typical example regions for each cluster identified in Nanostring. Nuclei are shown in blue, cholangiocyte epithelium in green, leukocytes in red, and tissue resident macrophages in yellow. Each circle is 660um in diameter. Complete NanoString ROIs are in **Extended Data Fig. 14**.

Figure 6. PSC macrophages are dysfunctional in cytokine secretion. A)

Representative flow plots of CD45⁺ (PTPRC⁺) and CD68⁺ cells in PSC, PBC and NDD TLH. B) PSC samples contained significantly fewer double positive cells ($p < 0.05$) in comparison to NDD and PBC. Percentage represents intact cells that are CD68⁺CD45⁺ in the PSC, PBC and NDD samples. C) *In silico* gating of scRNA-seq replicates decrease in CD68⁺CD45/PTPRC⁺ cells ($p=0.01$). D & E) Flow gating of CD45⁺CD68⁺ cells reveals increase in CD206⁺ subset in PSC ($P>0.05$). F & G) Following LPS stimulation, CD206⁺ PSC macrophages (CD45⁺CD68⁺) exhibit reduced production of TNF α ($p < 0.05$). Statistical significance for flow cytometry and intracellular cytokine staining is evaluated using a non-parametric Mann-Whitney U Test, *** $P < 0.001$, ** $P < 0.01$, * $P < 0.05$, error bars represent the standard error of the mean (SEM). Full gating strategy and unstimulated controls are shown in **Extended Data Fig. 19-20**.

Extended Data Fig. Captions

Extended Data Fig. 1 : Annotation of Coarse-level map. (A) Marker gene expression used to manually annotate 20 NDD liver clusters. (B) Pearson correlation between human hepatocyte clusters and zonation layers described in mouse (Halpern et al. 2017)). (C) Mouse hepatocyte zonation markers expressed in the annotated human map. (D & E) The map was divided into 8 major subgroups for subclustering.

Extended Data Fig. 2 : 38 cell-clusters defined in the healthy (NDD) liver. (A) top 5 markers

for each cell-cluster, known lineage markers are highlighted on the right. (B) UMAP depicting all 38 cell-types.

Extended Data Fig 3 : Subclustering of other populations of the NDD Map. (A) Endothelial cells. (B) Stellate / Mesenchymal cells (C) Cholangiocytes (D) Antibody secreting B cells. Left panels show UMAP of subclusters, Right panel shows top marker genes for each cluster.

Extended Data Fig. 4 : Subclustering of lymphocyte-like cells of the NDD Map. (A) UMAP of subclustered lymphocyte-like cells. (B) Marker genes of lymphocyte subtypes. (C i-iii) Subclustering of the proliferating cluster and annotation using the same markers as B. (D) Proportion of proliferating cells for each lymphocyte group based on C. (E) Differential pathway enrichments between cNK and IrNK cells from GSEA.

Extended Data Fig. 5: Subclustering of Macrophages (A) UMAP of integrated subclustered macrophages (B) Top marker genes for each cluster used to manually annotate the macrophage map. (C) Expression of conventional dendritic cell (cDC) markers. (D) Average expression of macrophage gene signatures from Guilliams et al 2022.

Extended Data Fig. 6 : Macrophage-LSEC interaction. (A) Expression of lineage specific genes in a random subset of doublet (grey), and singlet LSEC (orange) and macrophage (blue) cells confirms co-expression in the same droplet. (B) Most specific Monocyte-cvEndo interacting proteins as determined by CellPhoneDB. (C) Demonstrating colocalization of C1QC⁺ Kupffer cells and CD36⁺ LSECs, Central venous region in the healthy (NDD) liver by individual markers and fluorophores (DAPI, CD36-555 and C1QC-647), as well as merged. (D) Demonstrating the presence of CD9⁺ cells in the healthy (NDD) liver. Central venous region in the healthy (NDD) liver by individual markers and fluorophores (DAPI, CD36-555 and CD9-647), as well as merged.

Extended Data Fig. 7: Zonation of cell types in NDD liver. (A) First varimax principal component captures hepatocyte zonation in healthy liver spatial transcriptomics. (B) Top most contributing genes to the zonation associated component. (C) Example gene expression of a pericentral (GLUL) and periportal (HAMP) gene. (D - H) zonation score of individual marker genes for each of the major cell-types identified in the healthy map. Red = pericentral, blue = periportal. * $p < 0.01$, ** $p < 10^{-10}$, *** $p < 10^{-100}$.

Extended Data Fig 8. Immunofluorescence identifies bimodal distribution of VCAM1+ cells across the liver sinusoid. Red = VCAM1, Green = CD32, Blue = DAPI. (A) Individual sinusoids were divided into 10 layers from periportal (Layer 1) to central venous (Layer 10) regions. (B) Example images of a periportal, and (C) pericentral layer. (D) Quantification across 10 replicates. Statistical significance was assessed a one-way analysis of variance (ANOVA) with a Bonferroni post-test *** $P < 0.001$, ** $P < 0.01$, * $P < 0.05$. (E) Periportal region in healthy (NDD) liver by individual markers and fluorophores (DAPI, VCAM1-555 and CD32-647), as well as merged.

Extended Data Fig. 9: Disease-associated pathways in single-nucleus RNAseq.

(A) Significantly enriched pathways among genes differentially expressed between PSC and NDD livers (B) Significantly enriched pathways among genes differentially expressed between PBC and NDD livers (C) Pathways from A filtered to remove those also found in B. (D) Pathways from B filtered to remove those also found in A.

Extended Data Fig. 10: Integrated UMAP of cirrhosis liver data from Ramachandran et al. (2019). (A) Combined UMAP split by aetiology. (B) number of genes up (red) or down (blue) regulated in cirrhotic livers compared to uninjured livers in each cell-type. (C) frequency of each cell-type in each aetiology, due to small sample sizes, significance was tested comparing all cirrhotic to uninjured liver. (D) Cytokine expression in non-inflammatory cirrhotic liver. (E) Expression of hepatocyte and cholangiocyte marker genes from this study in the Ramachandran et al (2019) data. Note there was only 1 Hepatocyte captured in the PBC data thus it has been excluded.

Extended Data Fig 11. Immunofluorescence reveals increased CK7⁺HNF4A⁺ co-expressing cells in the PSC periportal area in comparison to the PBC and NDD liver. Periportal region by individual and merged protein markers: DAPI (blue), CK7 (red) and HNF4A (green) in (A) NDD, (B) PBC, and (C) PSC.

Extended Data Fig. 12: Cholestatic disease immune diversity captured in scRNA-seq. (A) number of genes up (red) or down (blue) regulated in PSC livers compared to NDD in each cell-type. (B) frequency of each cell-type in each aetiology, (i) rare cell-types that accounted for <1% of all the cells, (ii) cell-types accounted for ≥1%. Frequency of each cell-type among livers of each aetiology, significance obtained from wilcoxon rank sum test across sample: * p value < 0.05, ** p value < 0.01, ***p value < 0.001 (C) Proportion of doublets as estimated by Doublet Finder. (D) Expression of lymphocyte marker genes across T & NK cell populations.

Extended Data Fig. 13: Disease-associated pathways in single-cell RNAseq.

(A) Significantly enriched pathways among genes differentially expressed between PSC and NDD livers (B) Significantly enriched pathways among genes differentially expressed between PBC and NDD livers (C) Pathways from A filtered to remove those also found in B. (D) Pathways from B filtered to remove those also found in A.

Extended Data Fig. 14: 24 Nanostring Regions of Interest (ROIs). Images from the 24 regions of interest (ROIs) selected from the Nanostring GeoMx Digital Spatial Profiling platform. (A) PSC and NDD regions of interest in Slide 1 (PSC011_1-9, C71_1-4) and Slide 2 (PSC014_1-4, PSC018_1-6, C76_1-2). (B) Entire scanned Slide 1 (PSC011, C73) and Slide 2 (PSC014, PSC018, C76). White circles are 660um in diameter.

Extended Data Fig. 15. TGF-β is expressed in large scars where it co-localizes with Monocyte-like macrophages but not Kupffer cells. (A) Expression of the Monocyte-like macrophage marker S100A6 in VISIUM spatial transcriptomics of PSC liver. (B) Expression of TGF-β. (C) Annotated clusters in PSC. (D) Macrophage signature enrichments as calculated

using Giotto, using gene signatures for Kupffer (i) and Monocytes (ii) from Supplementary Table 2 within spatial transcriptomics of PSC liver. (iii) H&E stained tissue. Green arrows indicate scar areas.

Extended Data Fig. 16: Subclustering reveals macrophage diversity in PSC. (A)

Significantly enriched pathways among genes differentially expressed between PSC and NDD livers (B) Significantly enriched pathways among genes differentially expressed between PBC and NDD livers (C) Pathways from A filtered to remove those also found in B. (D) Pathways from B filtered to remove those also found in A.

Extended Data Fig. 17: Expanded CD45/CD68 and HLA-DR/CD206 flow cytometry plots.

A) Flow cytometry plots of CD68 vs. CD45 for NDD (n=5), PSC (n=4) and PBC (n=2) depicted in Figure 6A-B. B) Flow cytometry plots of HLA-DR vs. CD206 for NDD (n=5), PSC (n=4) and PBC (n=2) depicted in Figure 6D-E.

Extended Data Fig. 18: Expanded CD206/TNF α flow cytometry plots.

A) Flow cytometry plots of CD206/TNF α for unstimulated NDD (n=5), PSC (n=4) and PBC (n=2) TLH. B) Flow cytometry plots of CD206/TNF α for LPS and IFN γ stimulated NDD (n=5), PSC (n=4) and PBC (n=2) TLH depicted in Figure 6F-G.

Extended Data Fig. 19: Gating Strategies and FMOs (fluorescence minus one) for flow

cytometry immunophenotyping and intracellular cytokine staining of NDD (1-3) and PSC (1-3) TLH in Extended Data Fig. 17 and 18. A) Representative gating strategy of NDD sample. Gating on the immune fraction in a FSC-A vs SSC-A plot, followed by a gate include CD45⁺ cells in an FSC-A vs CD45 plot, followed by live cells based on a live/dead Zombie stain in an FSC-A vs Zombie plot, and then gating on CD45⁺CD68⁺ cells for macrophage analysis. B) CD45 and CD68 FMO plots used for the gating of CD68⁺CD45⁺ cells. C) CD206 and HLA-DR FMOs used to gate on CD206⁺ and HLA-DR⁺ cells. C) CD206 and TNF α FMOs used to gate on CD206⁺TNF α ⁺ cells.

Extended Data Fig. 20: Gating Strategies and FMOs (fluorescence minus one) for flow

cytometry immunophenotyping and intracellular cytokine staining of NDD (4-5), PSC (4), and PBC (1-2) TLH in **Extended Data Fig. 17 and 18**. A) Representative gating strategy of NDD sample. Gating on the immune fraction in a FSC-A vs SSC-A plot, followed by a gate include CD45⁺ cells in an FSC-A vs CD45 plot, followed by live cells based on a live/dead Zombie stain in an FSC-A vs Zombie plot, and then gating on CD45⁺CD68⁺ cells for macrophage analysis. B) CD45 and CD68 FMO plots used for the gating of CD68⁺CD45⁺ cells. C) CD206 and HLA-DR FMOs used to gate on CD206⁺ and HLA-DR⁺ cells. C) CD206 and TNF α FMOs used to gate on CD206⁺ TNF α ⁺ cells.

Extended Data Fig. 21: TGF- β incubation does not alter stimulation potential of NDD-derived myeloid populations.

Flow cytometry plots of CD206/TNF α for NDD TLH incubated for 24 hours with 0 ng/ml TGF- β (n=3), 10 ng/ml TGF- β (n=3) and 20 ng/ml TGF- β (n=3) A) without LPS and IFN γ stimulation, and B) with LPS and IFN γ stimulation. Flow cytometry plots

of HLA-DR/TNF α for NDD TLH incubated for 24 hours with 0 ng/ml TGF- β (n=3), 10 ng/ml TGF- β (n=3) and 20 ng/ml TGF- β (n=3), C) without LPS and IFN γ stimulation, and D) with LPS and IFN γ stimulation. E) Percentage of double positive population CD206⁺TNF α ⁺ across treatment conditions in B. F) Percentage of double positive population HLA-DR⁺TNF α ⁺ across treatment conditions in D. Gating strategy employed is described in Extended Data Fig 19 and 20.

Extended Data Fig. 22: Disease stage according to fibrosis was defined by the Nakanuma score and stage (29) assessing the following components: Fibrosis and Bile Duct Loss.

A) PSC advanced disease: Masson Trichrome stain assessed the extent of fibrosis and identified areas of scarring (stained in green) throughout the liver parenchyma and around individual bile ducts (concentric periductal fibrosis). B) PSC early disease: Early disease PSC livers showed less areas of fibrosis and prominent mononuclear cell inflammation surrounding individual bile ducts. C) Annotation of fibrotic areas (scars) within the liver parenchyma of explanted PSC tissue based on Masson Trichrome stain: The fibrotic areas (highlighted in green in Masson Trichrome Stain) are divided into a central and peripheral zone. The peripheral zone is defined as either the interface between periportal and zone 1 hepatocytes (1) or the periseptal zone of regenerative nodules (2) in cirrhotic liver parenchyma.

Extended Data Fig. 23: Cytokeratin 7 (CK7) immunohistochemical stain highlights hepatocytes with biliary metaplasia as a feature of chronic biliary disease within fibrotic areas (scars) in PSC explant livers. Bile duct epithelium is marked by a black arrow and metaplastic hepatocytes are marked by a yellow arrow, mainly at the periphery of fibrotic areas (scars).

A) PSC advanced disease: Low power view of Masson Trichrome Stain and immunohistochemical stain for CK7. B) PSC advanced disease: Intermediate power view of Masson Trichrome Stain and immunohistochemical stain for CK7. C) PSC advanced disease: High power view of Masson Trichrome Stain and immunohistochemical stain for CK7. D) PSC early disease: Low power view of Masson Trichrome Stain and immunohistochemical stain for CK7. E) PSC early disease: Intermediate power view of Masson Trichrome Stain and immunohistochemical stain for CK7. F) PSC early disease: High power view of Masson Trichrome Stain and immunohistochemical stain for CK7.

Supplementary Tables

Supplementary Table 1. Summary of Samples & Sequencing

Supplementary Table 2. Cell type specific markers identified in the NDD Liver map. These were determined through two-layer hierarchical clustering, first by clustering data into major cell-types as depicted in Figure 1, then by subclustering each of these clusters as shown in Extended Data Fig. 2-5. Marker genes for subclusters were determined in comparison to the other cells in the same coarse level cluster, not in comparison to the entire map. Log₂ fold-changes, P-values, and cluster information in this table presents the differential expression results for the most significant cluster when comparing the expression across all 38 cell-types in the entire map. Marker genes were selected based on specificity to each cell-type and expert knowledge in the field.

Supplementary Table 3. Summary of contributions of each sample to each cluster in the NDD Liver Map as well as PSC/PBC maps.

Supplementary Table 4. Cell-type specific differential expression between PSC or PBC and NDD using 5' scRNA-seq. DE was performed using pseudobulks and edgeR. Negative logFCs indicate genes upregulated in PSC/PBC and Positive logFCs indicate genes downregulated in PSC/PBC. Only genes passing 5% FDR multiple testing correction are included.

Supplementary Table 5. Cell-type specific differential expression between PSC and NDD using 3' snRNA-seq. DE was performed using pseudobulks and edgeR. Negative logFCs indicate genes upregulated in PSC and Positive logFCs indicate genes downregulated in PSC. Only genes passing 5% FDR multiple testing correction are included.

Supplementary Table 6. All cell-type markers from 5' PSC/PBC/NDD scRNA-seq. DE was performed using wilcox-rank-sum test.

Supplementary Table 7. All cell-type markers from 3' PSC/PBC/NDD snRNA-seq. DE was performed using wilcox-rank-sum test.

Acknowledgements

This publication is part of the Human Cell Atlas – www.humancellatlas.org/publications/. The authors acknowledge the Princess Margaret Genomics Centre, the Pathology Research Program and the Advanced Optical Microscopy Facility at University Health Network for their support and services. The graphical abstract and figures were created with Biorender.com. We would like to acknowledge PSC Partners Seeking a Cure Canada and Mary Vyas for patient partner participation in this project.

References

- [1] MacParland SA, Liu JC, Ma X-Z, et al. Single cell RNA sequencing of human liver reveals distinct intrahepatic macrophage populations. *Nat Commun* 2018;9:4383. <https://doi.org/10.1038/s41467-018-06318-7>.
- [2] Andrews TS, Atif J, Liu JC, et al. Single-Cell, Single-Nucleus, and Spatial RNA Sequencing of the Human Liver Identifies Cholangiocyte and Mesenchymal Heterogeneity. *Hepatol Commun* 2022;6:821–40. <https://doi.org/10.1002/hep4.1854>.
- [3] Guilliams M, Bonnardel J, Haest B, et al. Spatial proteogenomics reveals distinct and evolutionarily conserved hepatic macrophage niches. *Cell* 2022;185:379-396.e38. <https://doi.org/10.1016/j.cell.2021.12.018>.
- [4] Sharma A, Seow JJW, Dutertre C-A, et al. Onco-fetal Reprogramming of Endothelial Cells Drives Immunosuppressive Macrophages in Hepatocellular Carcinoma. *Cell* 2020;183:377-394.e21. <https://doi.org/10.1016/j.cell.2020.08.040>.
- [5] Kolodziejczyk AA, Federici S, Zmora N, et al. Acute liver failure is regulated by MYC- and microbiome-dependent programs. *Nat Med* 2020;26:1899–911. <https://doi.org/10.1038/s41591-020-1102-2>.
- [6] Ramachandran P, Dobie R, Wilson-Kanamori JR, et al. Resolving the fibrotic niche of human liver cirrhosis at single-cell level. *Nature* 2019;575:512–8. <https://doi.org/10.1038/s41586-019-1631-3>.
- [7] Atif J, Thoeni C, Bader GD, McGilvray ID, MacParland SA. Unraveling the complexity of liver disease one cell at a time. *Semin Liver Dis* 2022;42:250–70. <https://doi.org/10.1055/s-0042-1755272>.
- [8] Cheng ML, Nakib D, Perciani CT, MacParland SA. The immune niche of the liver. *Clin Sci* 2021;135:2445–66. <https://doi.org/10.1042/CS20190654>.
- [9] Karlsen TH, Folseraas T, Thorburn D, Vesterhus M. Primary sclerosing cholangitis - a comprehensive review. *J Hepatol* 2017;67:1298–323. <https://doi.org/10.1016/j.jhep.2017.07.022>.
- [10] Poch T, Krause J, Casar C, et al. Single-cell atlas of hepatic T cells reveals expansion of liver-resident naive-like CD4+ T cells in primary sclerosing cholangitis. *J Hepatol* 2021;75:414–23. <https://doi.org/10.1016/j.jhep.2021.03.016>.
- [11] Müller A-L, Casar C, Preti M, et al. Inflammatory type 2 conventional dendritic cells contribute to murine and human cholangitis. *J Hepatol* 2022. <https://doi.org/10.1016/j.jhep.2022.06.025>.
- [12] Pratt HE, Wu T, Elhajjajy S, et al. Beyond genome-wide association studies: Investigating the role of noncoding regulatory elements in primary sclerosing cholangitis. *Hepatol Commun* 2023;7. <https://doi.org/10.1097/HC9.0000000000000242>.
- [13] Zimmer CL, von Seth E, Buggert M, et al. A biliary immune landscape map of primary sclerosing cholangitis reveals a dominant network of neutrophils and tissue-resident T cells. *Sci Transl Med* 2021;13. <https://doi.org/10.1126/scitranslmed.abb3107>.
- [14] Chung BK, Henriksen EKK, Jørgensen KK, Karlsen TH, Hirschfield GM, Liaskou E. Gut and Liver B Cells of Common Clonal Origin in Primary Sclerosing Cholangitis-Inflammatory Bowel Disease. *Hepatol Commun* 2018;2:956–67. <https://doi.org/10.1002/hep4.1200>.

- [15] Henriksen EKK, Jørgensen KK, Kaveh F, et al. Gut and liver T-cells of common clonal origin in primary sclerosing cholangitis-inflammatory bowel disease. *J Hepatol* 2017;66:116–22. <https://doi.org/10.1016/j.jhep.2016.09.002>.
- [16] Guicciardi ME, Trussoni CE, Krishnan A, et al. Macrophages contribute to the pathogenesis of sclerosing cholangitis in mice. *J Hepatol* 2018;69:676–86. <https://doi.org/10.1016/j.jhep.2018.05.018>.
- [17] Reich M, Spomer L, Klindt C, et al. Downregulation of TGR5 (GPBAR1) in biliary epithelial cells contributes to the pathogenesis of sclerosing cholangitis. *J Hepatol* 2021;75:634–46. <https://doi.org/10.1016/j.jhep.2021.03.029>.
- [18] Govaere O, Cockell S, Van Haele M, et al. High-throughput sequencing identifies aetiology-dependent differences in ductular reaction in human chronic liver disease. *J Pathol* 2019;248:66–76. <https://doi.org/10.1002/path.5228>.
- [19] Wu S, Cao Y, Lu H, et al. Aberrant peribiliary gland niche exacerbates fibrosis in primary sclerosing cholangitis and a potential therapeutic strategy. *Biomed Pharmacother* 2022;153:113512. <https://doi.org/10.1016/j.biopha.2022.113512>.
- [20] Chen Y-Y, Arndtz K, Webb G, et al. Intrahepatic macrophage populations in the pathophysiology of primary sclerosing cholangitis. *JHEP Rep* 2019;1:369–76. <https://doi.org/10.1016/j.jhepr.2019.10.003>.
- [21] Kunzmann LK, Schoknecht T, Poch T, et al. Monocytes as potential mediators of pathogen-induced Th17 differentiation in patients with primary sclerosing cholangitis (PSC). *Hepatology* 2020. <https://doi.org/10.1002/hep.31140>.
- [22] Greenman R, Segal-Salto M, Barashi N, et al. CCL24 regulates biliary inflammation and fibrosis in primary sclerosing cholangitis. *JCI Insight* 2023;8. <https://doi.org/10.1172/jci.insight.162270>.
- [23] MacParland S, Ma X-Z, Manuel J, Liu J, Bader G, McGilvray I. Human Liver Caudate Lobe Dissociation for ScRNA-seq v2 2018. <https://doi.org/10.17504/protocols.io.m9sc96e>.
- [24] Nakib D, Perciani C, Chung S, et al. Human liver tissue storage methods for multiomic applications v1 2022. <https://doi.org/10.17504/protocols.io.261ge34qdl47/v1>.
- [25] Slyper M, Porter CBM, Ashenberg O, et al. A single-cell and single-nucleus RNA-Seq toolbox for fresh and frozen human tumors. *Nat Med* 2020;26:792–802. <https://doi.org/10.1038/s41591-020-0844-1>.
- [26] Lun ATL, Riesenfeld S, Andrews T, et al. EmptyDrops: distinguishing cells from empty droplets in droplet-based single-cell RNA sequencing data. *Genome Biol* 2019;20:63. <https://doi.org/10.1186/s13059-019-1662-y>.
- [27] Stuart T, Butler A, Hoffman P, et al. Comprehensive Integration of Single-Cell Data. *Cell* 2019;177:1888-1902.e21. <https://doi.org/10.1016/j.cell.2019.05.031>.
- [28] Korsunsky I, Millard N, Fan J, et al. Fast, sensitive and accurate integration of single-cell data with Harmony. *Nat Methods* 2019;16:1289–96. <https://doi.org/10.1038/s41592-019-0619-0>.
- [29] Frey BJ, Dueck D. Clustering by passing messages between data points. *Science* 2007;315:972–6. <https://doi.org/10.1126/science.1136800>.
- [30] Meilă M. Comparing Clusterings by the Variation of Information. In: Schölkopf B, Warmuth MK, editors. *Learning Theory and Kernel Machines*, vol. 2777, Berlin, Heidelberg: Springer Berlin Heidelberg; 2003, p. 173–87. <https://doi.org/10.1007/978-3-540-45167->

- 9_14.
- [31] Kiselev VY, Yiu A, Hemberg M. scmap: projection of single-cell RNA-seq data across data sets. *Nat Methods* 2018;15:359–62. <https://doi.org/10.1038/nmeth.4644>.
 - [32] Efremova M, Vento-Tormo M, Teichmann SA, Vento-Tormo R. CellPhoneDB: inferring cell-cell communication from combined expression of multi-subunit ligand-receptor complexes. *Nat Protoc* 2020;15:1484–506. <https://doi.org/10.1038/s41596-020-0292-x>.
 - [33] Robinson MD, McCarthy DJ, Smyth GK. edgeR: a Bioconductor package for differential expression analysis of digital gene expression data. *Bioinformatics* 2010;26:139–40. <https://doi.org/10.1093/bioinformatics/btp616>.
 - [34] Hernandez S, Lazcano R, Serrano A, et al. Challenges and Opportunities for Immunoprofiling Using a Spatial High-Plex Technology: The NanoString GeoMx® Digital Spatial Profiler. *Front Oncol* 2022;12:890410. <https://doi.org/10.3389/fonc.2022.890410>.
 - [35] MacParland SA, Tsoi KM, Ouyang B, et al. Phenotype Determines Nanoparticle Uptake by Human Macrophages from Liver and Blood. *ACS Nano* 2017;11:2428–43. <https://doi.org/10.1021/acsnano.6b06245>.
 - [36] Tsoi KM, MacParland SA, Ma X-Z, et al. Mechanism of hard-nanomaterial clearance by the liver. *Nat Mater* 2016;15:1212–21. <https://doi.org/10.1038/nmat4718>.
 - [37] Nakanuma Y, Zen Y, Harada K, et al. Application of a new histological staging and grading system for primary biliary cirrhosis to liver biopsy specimens: Interobserver agreement. *Pathol Int* 2010;60:167–74. <https://doi.org/10.1111/j.1440-1827.2009.02500.x>.
 - [38] Sarcognato S, Sacchi D, Grillo F, et al. Autoimmune biliary diseases: primary biliary cholangitis and primary sclerosing cholangitis. *Pathologica* 2021;113:170–84. <https://doi.org/10.32074/1591-951X-245>.
 - [39] Wang X, Perciani C, Ma X-Z, et al. Qupath digital quantification of liver immune cells v1 2021. <https://doi.org/10.17504/protocols.io.bs6gnhbw>.
 - [40] Dick SA, Wong A, Hamidzada H, et al. Three tissue resident macrophage subsets coexist across organs with conserved origins and life cycles. *Sci Immunol* 2022;7:eabf7777. <https://doi.org/10.1126/sciimmunol.abf7777>.
 - [41] Dick SA, Macklin JA, Nejat S, et al. Self-renewing resident cardiac macrophages limit adverse remodeling following myocardial infarction. *Nat Immunol* 2019;20:29–39. <https://doi.org/10.1038/s41590-018-0272-2>.
 - [42] Chakarov S, Lim HY, Tan L, et al. Two distinct interstitial macrophage populations coexist across tissues in specific subtissular niches. *Science* 2019;363. <https://doi.org/10.1126/science.aau0964>.
 - [43] Schiller C, Diakopoulos KN, Rohwedder I, et al. LST1 promotes the assembly of a molecular machinery responsible for tunneling nanotube formation. *J Cell Sci* 2013;126:767–77. <https://doi.org/10.1242/jcs.114033>.
 - [44] Kim J, Shapiro MJ, Bamidele AO, et al. Coactosin-like 1 antagonizes cofilin to promote lamellipodial protrusion at the immune synapse. *PLoS ONE* 2014;9:e85090. <https://doi.org/10.1371/journal.pone.0085090>.
 - [45] Zhao Y, Su H, Shen X, Du J, Zhang X, Zhao Y. The immunological function of CD52 and its targeting in organ transplantation. *Inflamm Res* 2017;66:571–8. <https://doi.org/10.1007/s00011-017-1032-8>.
 - [46] Jaitin DA, Adlung L, Thaiss CA, et al. Lipid-Associated Macrophages Control Metabolic

- Homeostasis in a Trem2-Dependent Manner. *Cell* 2019;178:686-698.e14. <https://doi.org/10.1016/j.cell.2019.05.054>.
- [47] Wen Y, Lambrecht J, Ju C, Tacke F. Hepatic macrophages in liver homeostasis and diseases-diversity, plasticity and therapeutic opportunities. *Cell Mol Immunol* 2021;18:45–56. <https://doi.org/10.1038/s41423-020-00558-8>.
- [48] Bonnardel J, T'Jonck W, Gaublomme D, et al. Stellate cells, hepatocytes, and endothelial cells imprint the kupffer cell identity on monocytes colonizing the liver macrophage niche. *Immunity* 2019;51:638-654.e9. <https://doi.org/10.1016/j.immuni.2019.08.017>.
- [49] Sasseti C, Tangemann K, Singer MS, Kershaw DB, Rosen SD. Identification of podocalyxin-like protein as a high endothelial venule ligand for L-selectin: parallels to CD34. *J Exp Med* 1998;187:1965–75. <https://doi.org/10.1084/jem.187.12.1965>.
- [50] Woodman RC, Johnston B, Hickey MJ, et al. The functional paradox of CD43 in leukocyte recruitment: a study using CD43-deficient mice. *J Exp Med* 1998;188:2181–6. <https://doi.org/10.1084/jem.188.11.2181>.
- [51] Klintman D, Li X, Thorlacius H. Important role of P-selectin for leukocyte recruitment, hepatocellular injury, and apoptosis in endotoxemic mice. *Clin Diagn Lab Immunol* 2004;11:56–62. <https://doi.org/10.1128/cdli.11.1.56-62.2004>.
- [52] Chung BK, Øgaard J, Reims HM, Karlsen TH, Melum E. Spatial transcriptomics identifies enriched gene expression and cell types in human liver fibrosis. *Hepatology* 2022;6:2538–50. <https://doi.org/10.1002/hep4.2001>.
- [53] Jameson G, Robinson MW. Insights into human intrahepatic NK cell function from single cell RNA sequencing datasets. *Front Immunol* 2021;12:649311. <https://doi.org/10.3389/fimmu.2021.649311>.
- [54] Yang C, Siebert JR, Burns R, et al. Heterogeneity of human bone marrow and blood natural killer cells defined by single-cell transcriptome. *Nat Commun* 2019;10:3931. <https://doi.org/10.1038/s41467-019-11947-7>.
- [55] Castellino F, Huang AY, Altan-Bonnet G, Stoll S, Scheinecker C, Germain RN. Chemokines enhance immunity by guiding naive CD8+ T cells to sites of CD4+ T cell-dendritic cell interaction. *Nature* 2006;440:890–5. <https://doi.org/10.1038/nature04651>.
- [56] Das H, Kumar A, Lin Z, et al. Kruppel-like factor 2 (KLF2) regulates proinflammatory activation of monocytes. *Proc Natl Acad Sci USA* 2006;103:6653–8. <https://doi.org/10.1073/pnas.0508235103>.
- [57] Peshkova IO, Fatkhullina AR, Mikulski Z, Ley K, Koltsova EK. IL-27R signaling controls myeloid cells accumulation and antigen-presentation in atherosclerosis. *Sci Rep* 2017;7:2255. <https://doi.org/10.1038/s41598-017-01828-8>.
- [58] Rückertl D, Hessmann M, Yoshimoto T, Ehlers S, Hölscher C. Alternatively activated macrophages express the IL-27 receptor alpha chain WSX-1. *Immunobiology* 2006;211:427–36. <https://doi.org/10.1016/j.imbio.2006.05.008>.
- [59] Damgaard RB, Walker JA, Marco-Casanova P, et al. The deubiquitinase OTULIN is an essential negative regulator of inflammation and autoimmunity. *Cell* 2016;166:1215-1230.e20. <https://doi.org/10.1016/j.cell.2016.07.019>.
- [60] Tiwari-Heckler S, Yee EU, Yalcin Y, et al. Adenosine deaminase 2 produced by infiltrative monocytes promotes liver fibrosis in nonalcoholic fatty liver disease. *Cell Rep* 2021;37:109897. <https://doi.org/10.1016/j.celrep.2021.109897>.

- [61] Letterio JJ, Roberts AB. Regulation of immune responses by TGF-beta. *Annu Rev Immunol* 1998;16:137–61. <https://doi.org/10.1146/annurev.immunol.16.1.137>.
- [62] Gindin Y, Chung C, Jiang Z, et al. A Fibrosis-Independent Hepatic Transcriptomic Signature Identifies Drivers of Disease Progression in Primary Sclerosing Cholangitis. *Hepatology* 2021;73:1105–16. <https://doi.org/10.1002/hep.31488>.
- [63] Guillot A, Winkler M, Silva Afonso M, et al. Mapping the hepatic immune landscape identifies monocytic macrophages as key drivers of steatohepatitis and cholangiopathy progression. *Hepatology* 2023. <https://doi.org/10.1097/HEP.000000000000270>.
- [64] Schaub JR, Huppert KA, Kurial SNT, et al. De novo formation of the biliary system by TGFβ-mediated hepatocyte transdifferentiation. *Nature* 2018;557:247–51. <https://doi.org/10.1038/s41586-018-0075-5>.
- [65] Sekiya S, Suzuki A. Hepatocytes, rather than cholangiocytes, can be the major source of primitive ductules in the chronically injured mouse liver. *Am J Pathol* 2014;184:1468–78. <https://doi.org/10.1016/j.ajpath.2014.01.005>.
- [66] Amatullah H, Fraschilla I, Digumarthi S, et al. Epigenetic reader SP140 loss of function drives Crohn's disease due to uncontrolled macrophage topoisomerases. *Cell* 2022;185:3232-3247.e18. <https://doi.org/10.1016/j.cell.2022.06.048>.
- [67] Fraschilla I, Amatullah H, Rahman R-U, Jeffrey KL. Immune chromatin reader SP140 regulates microbiota and risk for inflammatory bowel disease. *Cell Host Microbe* 2022;30:1370-1381.e5. <https://doi.org/10.1016/j.chom.2022.08.018>.

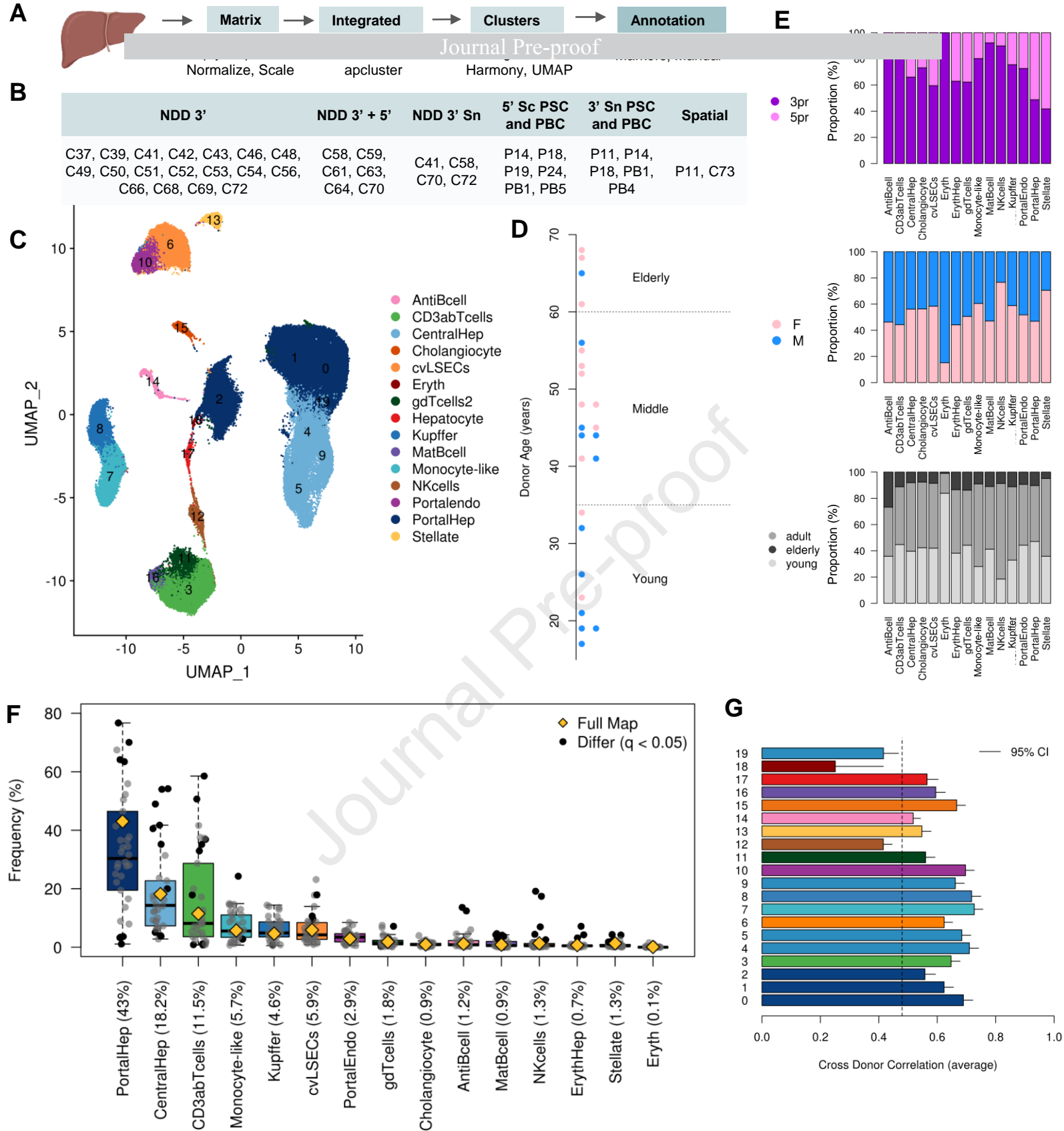


Figure 1: 100k single-cell map of NDD Human Liver reveals conserved cell-types across donors. (A) Single-cell RNAseq sample collection and analysis workflow (B) Table of samples sequenced in this study. (C) Integrated UMAP, containing 20 clusters annotated to 15 major cell-types (D) Age and sex profiles of the 24 donor livers pink = female, blue = male. (E) Proportion of cells from different technologies, sexes and ages contributing to each cell-type of the integrated data. Black points indicate significant enrichment / depletion ($p < 0.05$) based on a hypergeometric test using compositional analysis. There were no significant associations between demographic characteristics and the frequency of different cell-types. (G) Average correlation of the cluster profiles between different donors. The cluster profile is the mean expression of cells within that cluster. Dashed line indicates the average correlation between the cluster profiles of different clusters within the same donor.

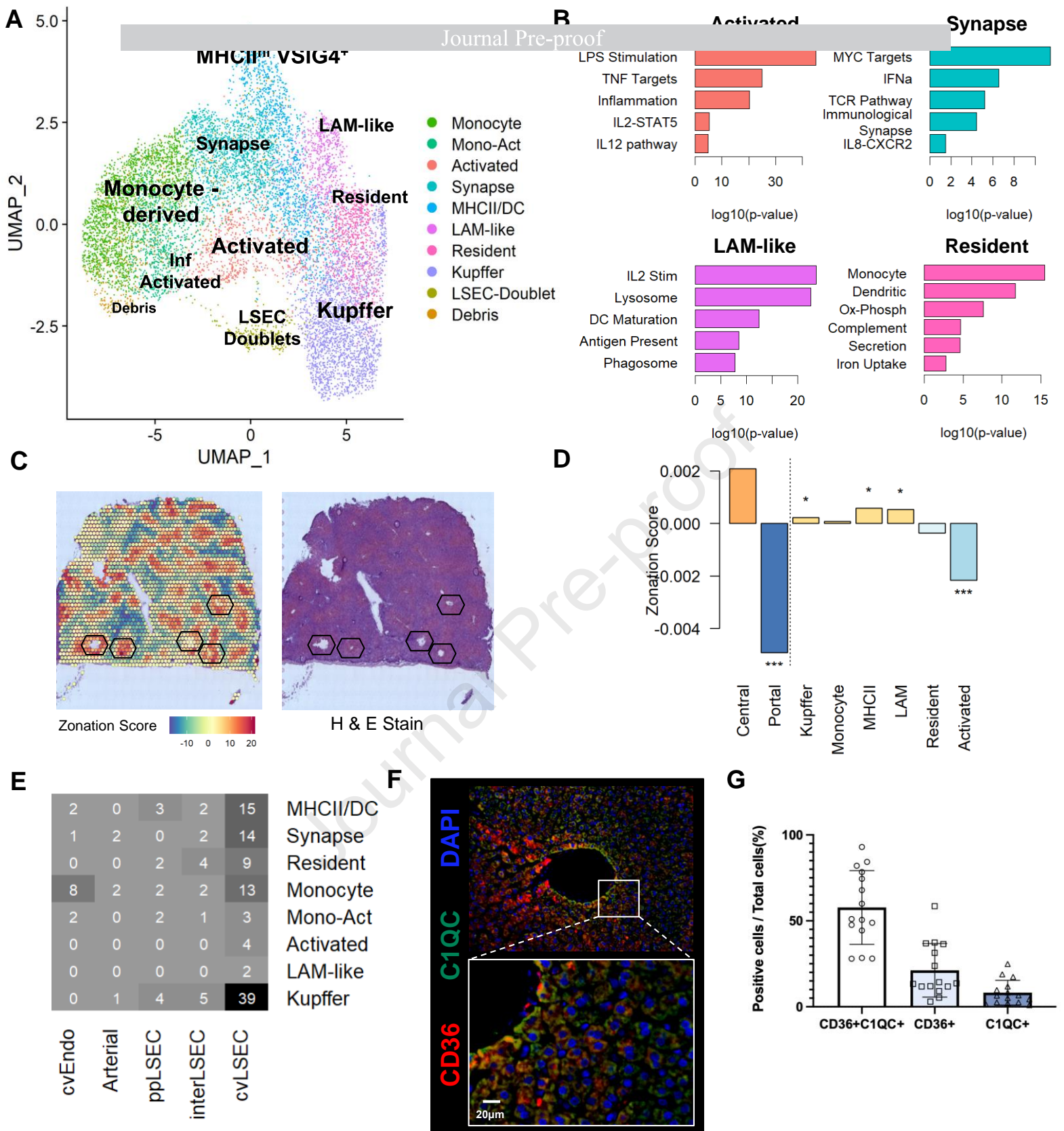


Figure 2: Macrophage diversity revealed by expanded NDD Liver map. (A) 11,127 macrophages were subclustered using Seurat and manually annotated to identify 10 distinct phenotypes. (B) Each subtype was enriched for distinct functional pathways as determined by GSEA. (C) Varimax PCA identifies a component that quantifies the zonation of each spot. Black hexagons indicate pericentral veins of distinct lobules. (D) Using the zonation score across four slices of spatial transcriptomics, we determine non-inflammatory macrophage populations are pericentral while activated macrophages are periportal. (E) Number of doublets assigned to each specific pair of subtypes using scmap. (F) Immunofluorescence of LSEC marker CD36 (red) and Kupffer cell marker C1QC (green) confirms presence of colocalized LSECs and Kupffer cells. (G) Percentage of cells over total cells that are co-expressing CD36+C1QC+, single positive CD36, and single positive C1QC.

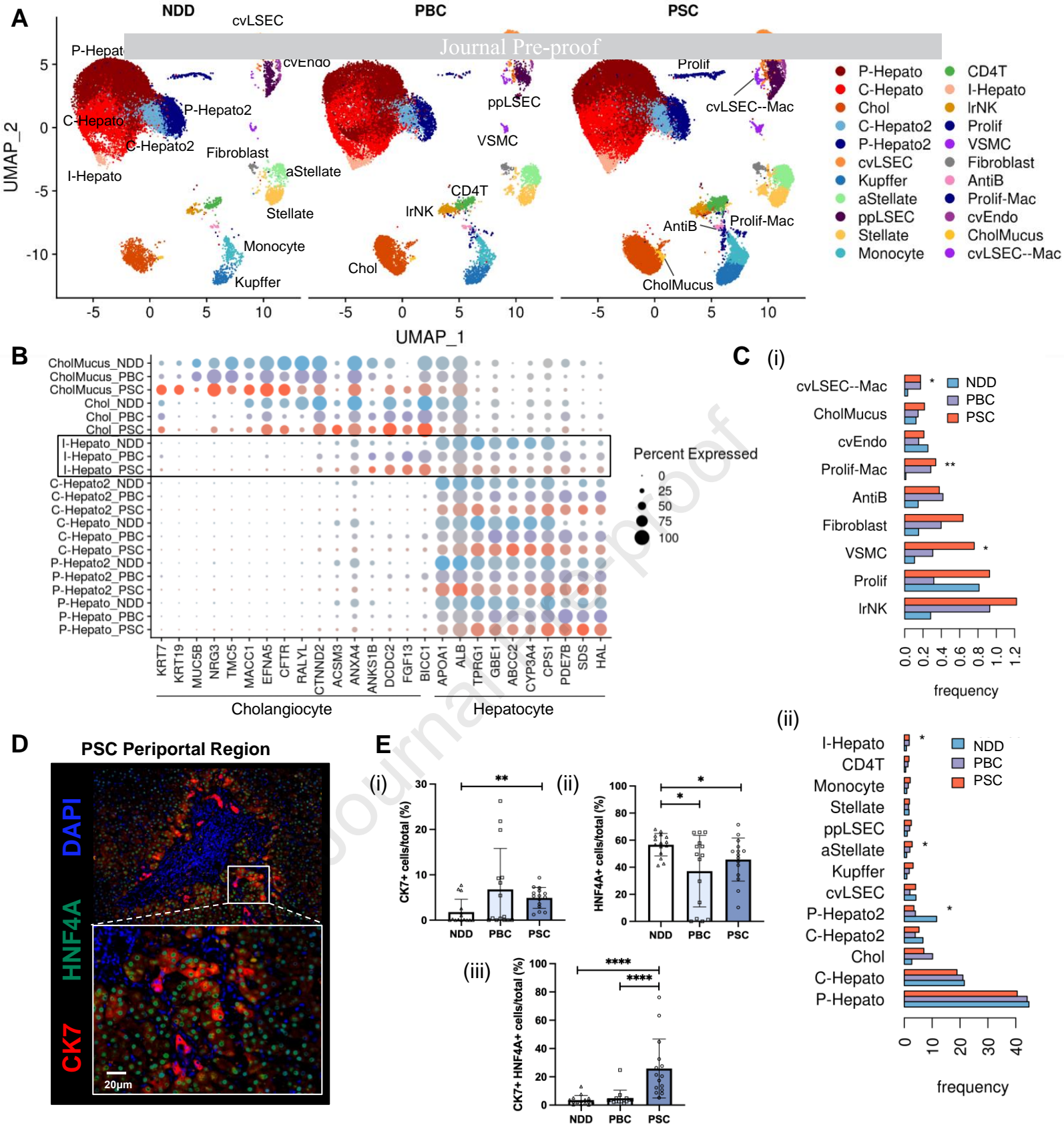


Figure 3: Hepatocyte transdifferentiation in biliary disease. (A) Integrated map of 24,511 NDD nuclei, 53,284 PSC nuclei, and 20,202 PBC nuclei. (B) Expression of hepatocyte and cholangiocyte markers across hepatocytes and cholangiocyte subtypes. (C) Frequency of each cell-type among livers of each aetiology, significance obtained from Wilcoxon rank sum test across sample: * p value < 0.05, ** p value < 0.01, ***p value < 0.001 (i) rare cell-types making up less than 1% of the total map. (ii) cell-types making up > 1% of the total map. (D) Representative IF image of a periportal (PP) region in the PSC liver. (E) Quantification of (i) CK7, (ii) HNF4A+, (iii) double CK7+HNF4A+ positive cells, significance obtained from Mann-Whitney test across samples: * P < 0.05, ** P < 0.01, *** P < 0.001, **** P < 0.0001.

Figure 4: Single-cell RNAseq reveals immunological complexity of PSC & PBC (A) Integrated map of 44,150 cells from PSC, 17,220 cells from PBC, and 24,007 NDD liver cells into a single map. (B) significantly enriched pathways obtained from gene set enrichment analysis (GSEA) on genes differentially expressed between PSC and NDD livers for each cell-type. (C) Expression of ligand-receptor pairs for known cytokines from the KEGG database in PSC, PBC, and NDD cells. Arrows indicate ligand to receptor relationships. (D) VISIUM spatial transcriptomics of key marker genes of immune populations. (i) naive B cells (ii) plasma B cells (iii-iv) CD4+T (v-vi) ppLSECs (vii-viii) hepatic stellate cells.

Journal Pre-proof

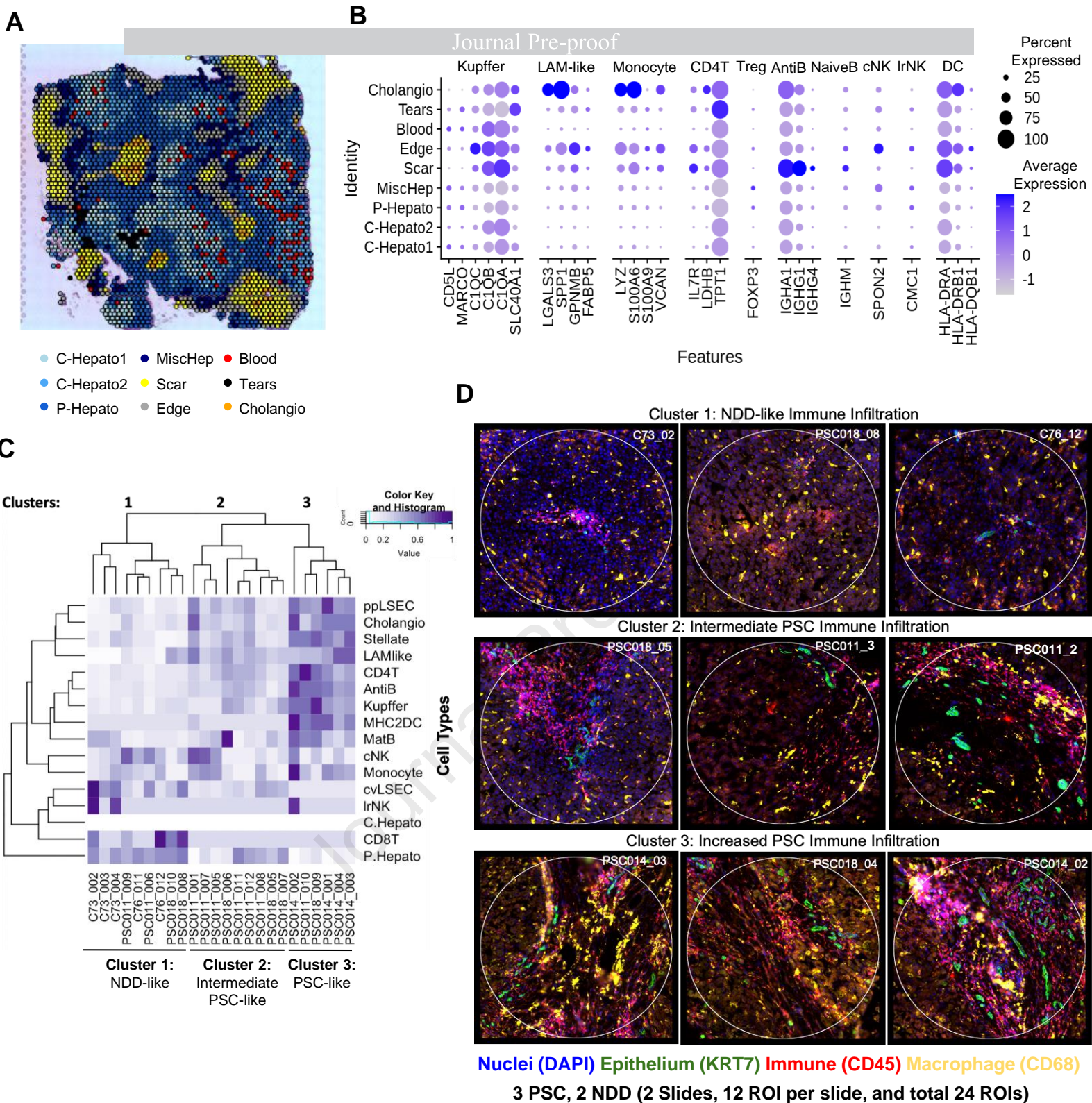


Figure 5: Enrichment of Immune cells in PSC (fibrotic areas) (A) Visium spatial transcriptomics was clustered and identified layers of distinct regions around fibrotic areas in PSC. (B) Expression of marker genes for each lymphocyte and macrophage subtype from the PSC and NDD single-cell maps in the PSC Visium data. LAMs and Monocytes were enriched in the core of scars near cholangiocytes and periphery of fibrotic areas, while B cells, T cells, and antigen presenting cells were enriched in the center of fibrotic regions, whereas NK cells present at the periphery. (C) Deconvolution of Nanostring digital spatial expression using cell-type markers from the NDD and PSC single-cell maps. (D) Images of typical example regions for each cluster identified in Nanostring. Nuclei are shown in blue, cholangiocyte epithelium in green, leukocytes in red, and tissue resident macrophages in yellow. Each circle is 660um in diameter. Complete NanoString ROIs are in Extended Data Fig. 14.

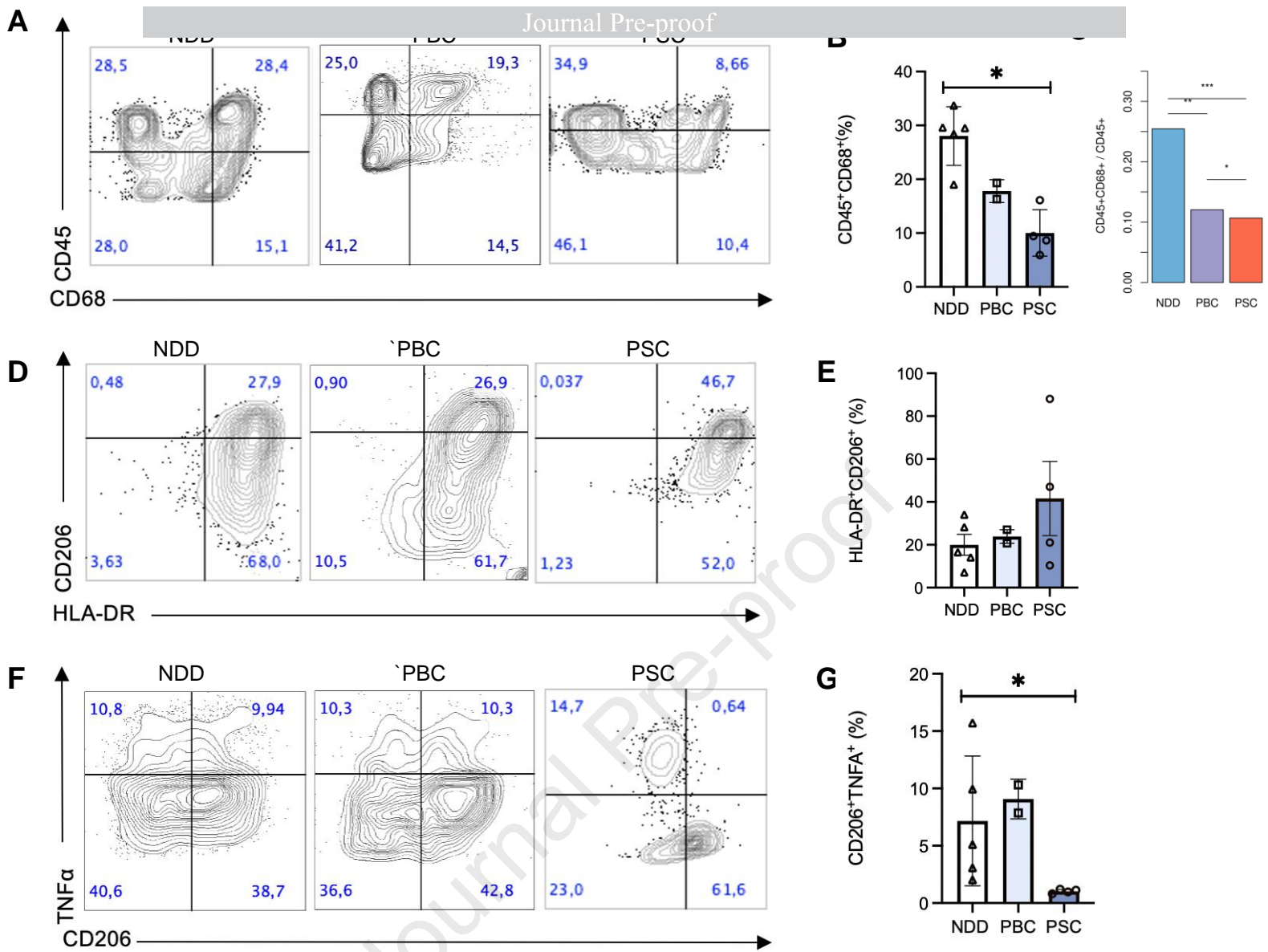


Figure 6. PSC macrophages are dysfunctional in cytokine secretion. A) Representative flow plots of CD45⁺ (PTPRC⁺) and CD68⁺ cells in PSC, PBC and NDD TLH. B) PSC samples contained significantly fewer double positive cells ($p < 0.05$) in comparison to NDD and PBC. Percentage represents intact cells that are CD68⁺CD45⁺ in the PSC, PBC and NDD samples. C) In silico gating of scRNA-seq replicates decrease in CD68⁺CD45⁺/PTPRC⁺ cells ($p=0.01$). D & E) Flow gating of CD45⁺CD68⁺ cells reveals increase in CD206⁺ subset in PSC ($P>0.05$). F & G) Following LPS stimulation, CD206⁺ PSC macrophages (CD45⁺CD68⁺) exhibit reduced production of TNF α ($p < 0.05$). Statistical significance for flow cytometry and intracellular cytokine staining is evaluated using a non-parametric Mann-Whitney U Test, *** $P < 0.001$, ** $P < 0.01$, * $P < 0.05$, error bars represent the standard error of the mean (SEM). Full gating strategy and unstimulated controls are shown in Extended Data Fig. 19-20.

Highlights

- ScRNA-seq revealed additional macrophage diversity in the NDD (healthy) liver.
- CD206⁺ macrophages in the PSC liver show reduced responsiveness to stimulation.
- CK7⁺ HNF4A⁺ transitioning hepatocytes are enriched in PSC fibrotic lesions in comparison to PBC and NDD.

Journal Pre-proof